DEVELOPMENT OF A HIGH-ORDER NAVIER-STOKES SOLVER FOR AEROACOUSTIC PREDICTIONS OF WIND TURBINE BLADE SECTIONS

A THESIS SUBMITTED TO
THE GRADUATE SCHOOL OF NATURAL AND APPLIED SCIENCES
OF
MIDDLE EAST TECHNICAL UNIVERSITY

BY

ÖZGÜR YALÇIN

IN PARTIAL FULFILLMENT OF THE REQUIREMENTS
FOR
THE DEGREE OF MASTER OF SCIENCE
IN
AEROSPACE ENGINEERING

AUGUST 2015

Approval of the thesis:

DEVELOPMENT OF A HIGH-ORDER NAVIER-STOKES SOLVER FOR AEROACOUSTIC PREDICTIONS OF WIND TURBINE BLADE SECTIONS

submitted by **ÖZGÜR YALÇIN** in partial fulfillment of the requirements for the degree of **Master of Science in Aerospace Engineering Department, Middle East Technical University** by,

Prof. Dr. Gülbin Dural Ünver
Dean, Graduate School of **Natural and Applied Sciences**

Prof. Dr. Ozan Tekinalp
Head of Department, **Aerospace Engineering**

Prof. Dr. Yusuf Özyörük
Supervisor, **Aerospace Engineering Department, METU**

Examining Committee Members:

Prof. Dr. İsmail Hakkı Tuncer
Aerospace Engineering Department, METU

Prof. Dr. Yusuf Özyörük
Aerospace Engineering Department, METU

Assoc. Prof. Dr. Sinan Eyi
Aerospace Engineering Department, METU

Prof. Dr. Mehmet Çalışkan
Mechanical Engineering Department, METU

Assist. Prof. Dr. Mustafa Kaya
Flight Training Department, UTAA

Date:

I hereby declare that all information in this document has been obtained and presented in accordance with academic rules and ethical conduct. I also declare that, as required by these rules and conduct, I have fully cited and referenced all material and results that are not original to this work.

Name, Last Name: ÖZGÜR YALÇIN

Signature :

ABSTRACT

DEVELOPMENT OF A HIGH-ORDER NAVIER-STOKES SOLVER FOR AEROACOUSTIC PREDICTIONS OF WIND TURBINE BLADE SECTIONS

Yalçın, Özgür
M.S., Department of Aerospace Engineering
Supervisor : Prof. Dr. Yusuf Özyörük

August 2015, 69 pages

Increased interest in renewable energy in the world has lead to research on wind turbines at a great pace. However, these turbines have come with a noise problem. The noise source of wind turbines is primarily aerodynamic noise highly related to complex, three dimensional, unsteady flow fields around them. Therefore, determination of these sources requires successful, accurate, turbulent flow solutions. In addition, because acoustic waves are non-dispersive and non-dissipative, such solutions must be carried out using low dissipation and low dispersion numerical schemes. Motivated by these points, a high order, parallel Navier-Stokes solver with 'dispersion-relation-preserving' (DRP) feature and delayed detached eddy simulation (DDES) capability has been developed. In this thesis, after the numerical methodology through this development is presented, some validation procedures are carried out in order to test order of accuracy, far field boundary conditions, inviscid and viscous flux routines, and DDES capability of the solver. Finally, the results of the turbulent flow structures causing noise around a NACA0012 blade section are demonstrated with the comparisons and comments.

Keywords: wind turbine noise, computational aeroacoustics, high-order methods, dispersion-relation-preserving, DDES

ÖZ

RÜZGAR TÜRBİNİ PAL KESİTLERİ İÇİN AEROAKUSTİK TAHMİNLER AMACIYLA YÜKSEK MERTEBELİ BİR NAVIER-STOKES ÇÖZÜCÜSÜNÜN GELİŞTİRİLMESİ

Yalçın, Özgür
Yüksek Lisans, Havacılık ve Uzay Mühendisliği Bölümü
Tez Yöneticisi : Prof. Dr. Yusuf Özyörük

Ağustos 2015 , 69 sayfa

Rüzgar enerjisine eğilimin artmasıyla birlikte rüzgar türbinleri üzerine yapılan araştırma ve geliştirmeler de artmıştır. Fakat, bu türbinlerin kullanımı gürültü sorununu da beraberinde getirmiştir. Aerodinamik gürültü, rüzgar türbini gürültü bileşenleri içinde çok önemli yer teşkil eder. Bu gürültüye türbin palleri etrafındaki üç boyutlu, karmaşık ve durağan olmayan akışlar sebep olur. Bu nedenle paller etrafındaki gürültü oluşma ve yayılma benzetimi yüksek doğruluk dereceli ve başarılı türbülans hesaplamaları gerektirir. Akustik dalgaların kayıpsız ve dağılmadan ilerlemesini benzetmek için bu hesaplamalar yüksek mertebeli ve dağılma ilişkisini koruyan çözüm şemaları kullanılarak yapılmalıdır. Bu amaç doğrultusunda yüksek mertebeli, 'dağılma-korunumu-prensibi'ne uygun, DDES benzetim kapasiteli, paralleştirilmiş bir Navier-Stokes çözücüsü geliştirilmiştir. Bu çalışmada önce çözücünün geliştirilmesi sırasında kullanılan yöntemler tanıtılmakta, sonrasında ise doğrulama amacı ile bazı hesap rutin testleri yapılmaktadır. Çalışmanın sonunda NACA0012 pal kesiti etrafında gürültüye sebep olan akış sonuçları, kıyas ve yorumlar eşliğinde sunulmaktadır.

Anahtar Kelimeler: rüzgar türbini gürültüsü, hesaplamalı aeroakustik, yüksek-mertebeli yöntem, dağılma-korunumu-prensibi, DDES

To people who are deeply occupied with freedom of their land ...

ACKNOWLEDGMENTS

Öncelikle danışmanım Yusuf Özyörük'e henüz yüksek lisans eğitimim başlamamışken bana güvenerek yürütmekte olduğu Tübitak projesine beni dahil ettiği ve bu tez konusuna beni teşvik ettiği için çok teşekkür ederim. Bu çalışmamın başından sonuna kadar ihtiyacım olduğu her anda bana zaman ayırdığı ve karşılaştığım her problemde yardımını hiç esirgemediği için kendisine minnettarım.

Tez sürecimin her aşamasında bana destek olan, tecrübelerini aktaran, sorunlarımı büyük bir sabırla dinleyen ve tıkandığım her noktada bana yol gösteren Kenan Cengiz'e çok teşekkür ederim.

3 yıllık tez sürecimin her bir yılında ayrı ayrı odamı paylaştığım asistan arkadaşlarım Özgür Tümüklü, Emre Yılmaz ve Arda Akay'a güzel bir çalışma ortamı yarattıkları, dertlerime ve heyecanlarıma ortak oldukları için çok teşekkür ederim.

Tez sürecim boyunca akademik anlamda bana desteğini esirgemeyen tüm araştırma görevlisi ve proje çalışanı arkadaşlarıma ayrı ayrı teşekkür ederim. Ayrıca dostluklarını hep yanımda hissettiğim, her sabah çalışmaya güler yüzlü ve motive bir şekilde başlamamı sağlayan Özgür Harputlu, Özcan Yırtıcı, Pınar Eneren, Kenan Cengiz, Emre Yılmaz, Arda Akay, Oğuz Onay, Sinem Özçakmak, Özgür Tümüklü, Emrecan Suiçmez ve Muharrem Özgün'e çok teşekkür ederim.

Lisans hayatımdan itibaren her şeyimi paylaştığım, çok güzel vakit geçirdiğim, birlikte sabahladığım, birlikte mezun olduğum Havacılık Tayfa'ya ayrı ayrı teşekkür ederim. İyi ki varsınız!

Eğitim hayatımın başından itibaren her zaman beni destekleyen ve bana duydukları güveni hiç yitirmeyen anneme, babama ve tüm aileme çok ama çok teşekkür ederim. Her an benimle üzülen, benimle sevinen, varlığını hep yanımda hissettiğim annemin elde ettiğim tüm başarı ve aldığım tüm diplomalarda en az benim kadar katkısı vardır.

Son 1.5 senemin her anını paylaşmaktan mutluluk duyduğum, en sıkıntılı anlarımda sevgisini ve desteğini hep yanımda hissettiğim, huzurlu ve mutlu bir tez süreci yaşamamı sağlayan, sevgilim Hazal'a çok çok teşekkür ederim.

Son olarak, tezime sağladığı teknik destekten dolayı RÜZGEM'e ve 3 yıl boyunca 112M106 numaralı TÜBİTAK1001 projesi vasıtasıyla desteğini sürdüren TÜBİTAK kurumuna teşekkür ederim.

TABLE OF CONTENTS

CHAPTERS

APPENDICES

LIST OF TABLES

TABLES

LIST OF FIGURES

FIGURES

LIST OF ABBREVIATIONS

HAWT	Horizontal Axis Wind Turbine
VAWT	Vertical Axis Wind Turbine
CAA	Computational Aeroacoustics
CFD	Computational Fluid Dynamics
DRP	Dispersion-Relation-Preserving
NS	Navier-Stokes
FW-H	Ffowcs Williams-Hawkings
FV	Finite Volume
FD	Finite Difference
RK	Runge-Kutta
LM	Linear Multistep
LDDRK	Low Dissipation Dispersion Runge-Kutta
PML	Perfectly Matched Layer
DNS	Direct Numerical Simulation
RANS	Reynolds-Averaged Navier-Stokes
URANS	Unsteady Reynolds-Averaged Navier-Stokes
LES	Large Eddy Simulation
DES	Detached Eddy Simulation
MSD	Modelled-Stress Depletion
DDES	Delayed Detached Eddy Simulation
SA	Spalart-Allmaras
ρ	density
u,v,w	velocity components
V	velocity vector
M	Mach number
p	pressure
Re	Reynolds number
e_t	total energy

T	temperature
x,y,z	axes of Cartesian coordinates
ξ, η, ζ	axes of Curvilinear coordinates
γ	specific heat ratio
Pr	Prandtl number
τ	shear stress
q	heat flux
μ_{dyn}	molecular dynamic viscosity
μ_{turb}	turbulent eddy viscosity
ν	molecular kinematic viscosity
$\tilde{\nu}$	turbulent flow variable
α	wavenumber
ω	angular frequency
a_j	DRP coefficients in space domain
b_j	DRP coefficients in time domain
β_j	RK coefficients in time domain
c_j	DRP coefficients in space domain for artificial dissipation
μ_{ad}	weight of artificial dissipation
$\tilde{n}$	surface normal vector
R	gas constant
∇	gradient operator
Δ	difference operator
δ_{ij}	Kronecker delta
( )'	fluctuation flow variables
$(\,)_\infty$	freestream flow variables
JST model	Jameson Schmidt Turkel model
$\mathcal{L}_{AD}$	artificial dissipation operator
ϵ	weight of JST model
D_ξ	discretization operator in ξ direction
H	Heaviside function
δ	Dirac delta function
Q, F_i, T_{ij}	monopole, dipole, quadrupole source terms
$(\,)_0$	flow variables far from the FW-H surface
G	Green function

β	Prandtl-Glauert factor
I/O	Input/Output
C_p	pressure coefficient
C_f	friction coefficient

CHAPTER 1

INTRODUCTION

1.1 Wind as a Renewable Energy

Renewable energy has recently become one of the most attractive topics around the world because of global concerns such as climate change, overpopulation and energy deficiency. In the mean time, gradually increment of global energy requirement which will be in 2040 almost 1.5 times higher than 2010 [16] raises the importance of these concerns. The three positive contributions of renewable energy are reduction of dependence on infrequent and expensive fossil fuels, protection of global climate and creation of new international markets via green industries. Consequently, governments are being forced to change their energy policies through renewable energy by intergovernmental organizations (e.g. IRENA - International Renewable Energy Agenda [29]) and international treaties and policies (e.g. Kyoto Protocol and Copenhagen Accord [35, 1]).

Among renewable energy sources like solar, biomass, geothermal and others [6], wind is accepted as one of the leading energy source and wind turbines are the most common tools to extract energy from it. Increased interest in renewable energy in the world, therefore, has lead to installation of wind turbines at a great pace which can be supported by the wind market statistics of Global Wind Energy Council - GWEC [23] (see Figure 1.1).

On the other hand, increase in both installed wind capacity and residential areas due to overpopulation has caused a conflict such that people living nearby wind farms have started to complain about wind turbine noise. It is reported that wind turbine

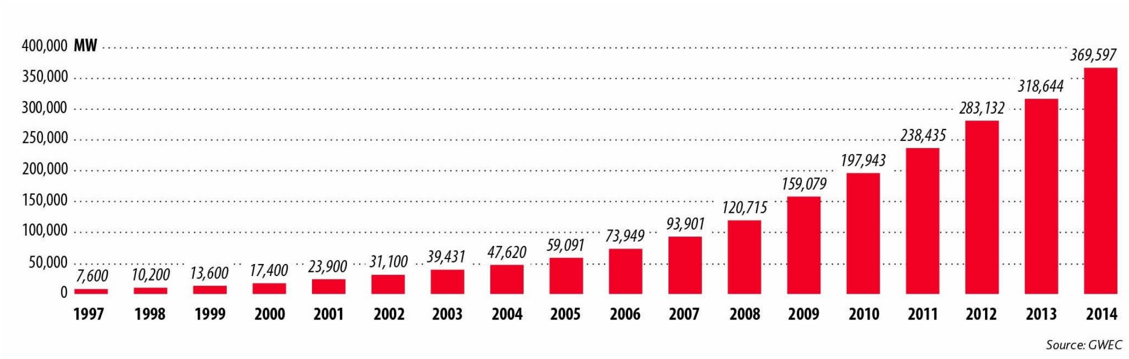

Figure 1.1: Global Cumulative Installed Wind Capacity (1997-2014) [23]

noise could be sensed as far as 1.5 km away [51, 41]. Furthermore, it could be more annoying than transportation noise [51, 49]. For example, a 10 kW small wind turbine build for residential power can cause a 60 dB sound pressure level with a wind speed of 6 m/s. However, when wind speed is increased to 13 m/s, the sound pressure level increases over 13 dB and approaches to a noise level caused by a street traffic [53]. Although there is no international noise regulations and standards, some European countries have limited noise levels to around 40 dB for the wind turbines near the residential areas [53]. Moreover, this annoyance grows especially at night since approximately 15 dB higher noise levels can be reached than in daytime [67]. Therefore, it can be said that while usage of wind energy has become widespread and popular, it has come with a noise problem.

1.2 Noise Sources of Wind Turbines

Wind turbines are classified according to their rotor axis arrangement as Horizontal Axis Wind Turbines (HAWT) and Vertical Axis Wind Turbines (VAWT). Power generation of wind turbines could be increased with the length of the blades [68]. Since generator and transmission devices of VAWTs are located on ground, the size of these turbines could not be extended as much as HAWTs. Therefore, trend of an installation of wind turbines for generating much more energy goes through the HAWT technology. Hence, the noise problem of horizontal axis ones forms the biggest part of the acoustic researches on wind turbines.

The noise source related to wind turbines is of aerodynamic and mechanic origin in principle. Mechanical noise, also called hub noise, is caused from the mechanical parts especially gearbox in the hub region. However, this kind of noise is achieved to be reduced as enhancement of technology [46]. Nowadays in modern turbines, aerodynamic noise, also called blade noise, is higher than hub noise [53]. Sound levels for broadband frequency domain (Figure 1.2(b)) and projection of the measured noise sources averaged over several rotations (Figure 1.2(a)) are used to demonstrate this comparison in experimental studies [44]. Hence, the wind turbine noise issue has been regarded as an aeroacoustic problem.

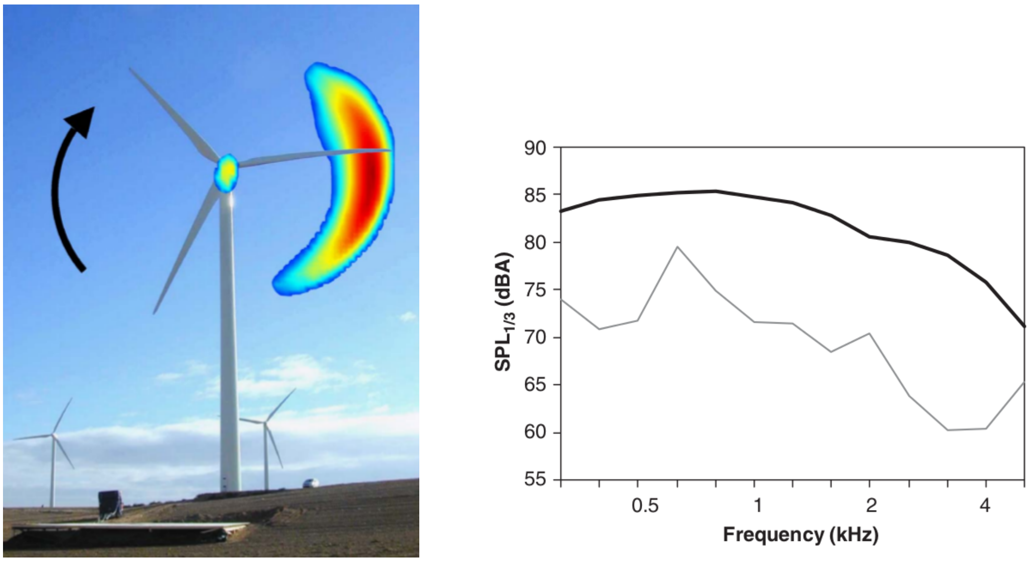

(a) Projection of noise sources averaged over several rotations

(b) Averaged spectra of hub (—) and blade noise (**—**)

Figure 1.2: Comparison of blade and hub noise [44]

Noise emitted from a rotary blade is generally created by three types of sources; monopole, dipole, and quadrupole. While displacement of the blade volume due to rotation causes monopole sources, steady aerodynamic loadings on the blade surface cause dipole sources. On the other hand, turbulent flow around the blade causes quadrupole sources. While monopole and dipole sources emit low and discrete sound components, quadrupole sources cause broadband noise emissions. Quadrupole sources are more significant for the wind turbine blades due to its low speed nature [70, 53]. Noise sources caused by turbulent flow is shown in Figure 1.3. Unlike the turbulent flow developed by the blade itself (known as self-noise in literature), interaction of oncoming atmospheric turbulent flow with the leading edge of the blade creates a dipole source (low-frequency noise, up to 160 Hz frequency). The reason is that the interaction caused an unsteady lift which means an aerodynamic loading on the blade surface. The other sources shown in Figure 1.3 are due to a blade boundary layer which is arisen from the flow progression over the large wind turbine blades.

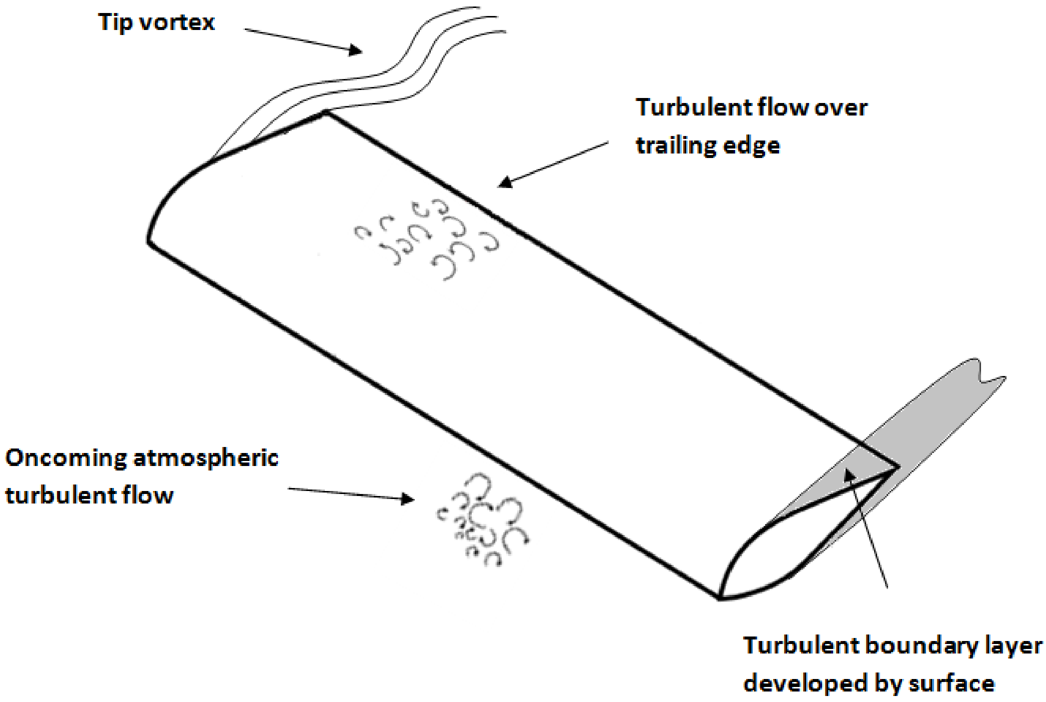

Figure 1.3: Aerodynamic noise sources over a blade

Turbulent fluctuations do not emit noise themselves in an efficient way. However, when they interact with a sharp trailing edge as in the wind turbines, vortical motions related with near field pressure disturbances are created. Thus, these interactions cause broadband noise emission which is in a range of 160-1500 Hz frequency values and this is why trailing edge noise is believed as the most important noise source in the wind turbines [45].

Apart from the turbulent flow, there is a vortex shedding noise caused by laminar boundary layers (also called a tonal noise). It becomes influential at low Reynolds numbers. Hence, for large wind turbines where flow with high Reynolds numbers takes part, it is not a threatening problem [15].

Another source to be mentioned lastly is the blade tip noise. It occurs due to the pressure difference between top and bottom surfaces of the blade which generates a trailing vortex at the tip of the blade. As wind turbines are getting bigger and bigger, this topic has become as important as the interaction of turbulent boundary layer - trailing edge interaction noise [46].

In brief, noise sources due to flow around a rotary blade are summed up in Table 1.1:

Table 1.1: Noise source types in aerodynamic origin for a rotary blade

Source Types	**Directivity**	**Frequency Range**
Displacement of the blade volume	Monopole	Low
Aerodynamic loadings on the blade surface	Dipole	
Interaction of the leading edge and the oncoming turbulence		
Interaction of the turbulent boundary layer and the trailing edge	Quadrupole	Broadband
Blade tip noise		
Laminar boundary layer vortex shedding (tonal noise)		

1.3 Methods for Noise Source Detection

It is certain that determination of the noise source locations and types accurately is crucial to be able to solve the noise issue during the design process of the wind turbines. In this regard, much research on wind turbine noise sources are carried out experimentally [22, 32, 44], computationally [20, 60] or semi-theoretically and theoretically (acoustic analogy) [4]. Determination experimentally is for sure the most reliable method if the test environment could be impeccable. However, test set-up for the wind turbines is quite difficult; for instance, pureness of the blade surfaces, mounting and positioning the microphone platform, control of the oncoming air flow are some of the considerations to be certainly prepared and arranged in a studious way.

Computational way to detect the wind turbine noise sources implies basically a numerical simulation of the fluid motions in acoustic frame. This is regarded as Computational Aeroacoustic simulations (CAA). As previously mentioned, most noise sources are associated with turbulent structures (eddies) and the turbulent flow is composed of random, three dimensional, non-linear and unsteady fluid motions as it is well known. Therefore, due to its complexity, a proper resolution of turbulent flow is needed for accurate noise simulations. Although there are commonly used commercial flow solvers (such as [2, 7]) with the capability of flow simulation over a rigid body, they are more suitable for steady-state flow solutions and flows changing slowly in time due to low-order numerical schemes employed (mostly second order). For acoustic purposes high-order numerical methods are needed [66] for low dissipation and dispersion errors. This argument will be discussed in details in Chapter 1.4. Furthermore, even very vortical flow motions can radiate less sound compared with its total energy especially at low Mach numbers because the noise sources may cancel each other during long propagations. By considering this information, if any numerical solver causes large computational errors, it may estimate more noise at far regions than it should be [11]. Thus, truncation error should also be handled seriously during CAA simulations.

Acoustic analogy, on the other hand, is the first theory to discuss and demonstrate that the reason of the aerodynamic noise is the flow itself [37]. This analogy basically shows a derivation of a classical wave equation, that has source terms (Lighthill's stress tensor) on the right hand side and perturbation terms on the left hand side, from Navier-Stokes (NS) equations with some mathematical operations. Since the source terms are represented by the turbulent fluctuations, the flow region is treated as the acoustic environment. Then, when the governing equation is solved by Green Function [18], it is seen that the solution is directly associated with the turbulent flow region. On the other hand, since directly numerical computations of all the regions from source location to the far away fields is still expensive, acoustic analogy is preferred to estimate the noise sensed by a far away observer by integral techniques after obtaining the numerical solution at near fields. The widely-used integral approaches are Kirchhoff [34] and Ffowcs Williams-Hawkings (FW-H) [72] equations. They can both handle the source terms on moving surfaces with the turbulent flow effects. Although Kirchhoff method is mostly applicable in a surface that is in linear flow region, its area of utilization is extended by many studies such as ducted fan problems by Özyörük and Long [47], jet problems by Shih et al. [40] and others.

However, when the integration surface is in non-linear flow regions, FW-H method can estimate the radiated sound more properly than Kirchhoff method [55]. Furthermore, FW-H equation is well-suitable for the helicopter and wind turbine blade noise calculations from the domain of the flow solutions near the solid body to the far away regions effectively [60, 18].

1.4 Computational Issues

Sound is composed of acoustic waves that are non-dissipative, and non-dispersive in non-convective mediums, and propagate with the local speed of sound. For this reason, acoustic waves can propagate in any direction (contrary to entropy and vorticity waves) without attenuation over long distances. Numerical methods for aeroacoustic problems, therefore, must provide low dissipation, low dispersion characteristics of the noise and this subject constitutes the main difference between CAA and CFD (Computational Fluid Dynamics) problems.

Dissipation error is an amplitude error which means a mismatch between the amplitude of the wave solved by numerical discretizations and that of the physical (actual) wave. On the other hand, dispersion error emanates from phase speed or frequency distinctness between numerical and actual waves. As known that low-order algorithms are inherently dissipative and therewithal could not capture dispersion relation accurately. That is why high-order numerical algorithms are required in CAA problems.

Although central schemes can be dispersive, they do not produce dissipation in computational domains. Non-central schemes (like upwinding) conversely cause dissipation and therefore they are usually avoided to use in CAA simulations. Nevertheless, some studies (such as [76, 25]) do not hesitate to use non-central schemes because dissipative terms are necessary for damping out the unnatural short waves emerged from the high-order discretizations of the partial differential equations. For instance, much amount of dissipation must be included in numerical algorithms for the steady-state solutions or shock capturing problems. However, both satisfying the wave propagation characteristics of sound and removing these spurious waves may become a pretty difficult and highly noteworthy situation to be applied in CAA simulations. The reasons are that unsteady acoustic problems include long propagations of noise disturbances and dissipation causes spatially altering solutions of amplitude and phase of the waves. Although these non-central algorithms are trying to rearrange the mesh stencil sizes to overcome excessive dissipation [76], central schemes are also be preferred with explicitly addition of artificial dissipation terms. These terms eliminate the contamination of spurious short waves from the computational domains without damping the low frequency waves (with high wavelengths) when dissipation is required especially at physical boundaries. The methodology of artificial dissipation algorithm will be widely mentioned in Chapter 2.4.

Statement of the wave propagation theory is that the number of wave modes (acoustic, vorticity and entropy) and the wave propagation characteristics (isotropic, non-dissipative and non-dispersive) are expressed by the dispersion relations of the governing equations [71]. Hence, this theory helps to understand that any numerical discretizations should avoid to damage dispersion relations of the partial differential equations to be used. In accordance with this purpose, the 'dispersion-relation-preserving' (DRP) scheme by Tam and Webb [64] has opened a new road in 1990s to aeroacoustic problems. They proposed high-order finite difference methods to provide not only a low dissipation feature in numerical solutions but also almost a match between the exact dispersion relation of the governing differential equations and the numerical one. The idea behind this algorithm is preserving the Fourier transforms of the partial differential equations since the dispersion relations are obtained by taking the Fourier transforms of these equations. Therefore, DRP discretizations in both space and time domains were derived in this manner. This novel algorithm has been extant in many CAA applications.

1.4.1 Finite Difference Solver

For numerical solvers developed for aeroacoustic purposes, obtaining high-order accuracy is a must. While creating a mesh domain, the use of unstructured grids are more suitable to handle difficulties of the complex geometries than structured ones. However, it is not easy to achieve a high-order accuracy with unstructured ones during spatial discretizations. Moreover, for a wind turbine blade section simulation, it is enough to use structured grids providing that the mesh quality. On the other hand, although finite volume (FV) approach could be implemented to unstructured grids in a more appropriate way than finite difference (FD) methods, the use of FD methods are adequate for a non-complex geometry as in this thesis, regarding their easy implementation.

1.4.2 Time Integration Methods

To be able to provide less dissipative and less dispersive scheme, temporal discretization must also be applied accordingly. For explicit FD solvers, Runge-Kutta (RK) and Linear Multistep (LM) time integration methods are generally preferred [10]. RK methods do the time integration by dividing the time step in stages and compute a variable one time step further from the obtained information of each stages. On the other hand, LM methods use the information from the prior time steps to go forward in time. As examples through acoustic purpose, while Tam and Webb developed a LM method with DRP scheme [64], Hu et al. optimized the RK methods to get low dissipation and low dispersion features (called as LDDRK [26]).

1.4.3 Considerations for Outer Boundary

High accurate numerical algorithms are mandatory but not sufficient by themselves for CAA problems. The use of these algorithms becomes meaningful with appropriate boundary conditions. Since acoustic waves, during propagation, decline so slowly than other flow disturbances, outgoing from the computational boundaries without reflection should be treated more attentively than CFD simulations. This also shows why CAA applications differ from CFD ones. For this purpose, some non-reflecting artificial boundaries have been improved. Asymptotic boundary conditions [3, 64], characteristic boundary conditions [21, 50], and Perfectly Matched Layer (PML) technique [27, 24] can be shown as examples of famous non-reflecting boundary types. Among them, asymptotic ones are considered as the most reliable ones for wide scale CAA problems [10, 36] only if the artificial boundary is constituted adequately far from the body to be simulated.

1.5 Turbulence Modelling Issues

Up to now, the importance of an accurate numerical solver of turbulent fluctuations to predict aerodynamic noise caused by wind turbine blades and the computational considerations while creating this solver have been discussed in Chapter 1.2 and Chapter 1.4. Besides, selection of the governing equations is another remarkable point. As is known to all, fluid motion is basically identified with NS equations. However, the governing equations to be solved are changing with the type of the acoustic problems. For example, while it is sufficient to describe linear wave propagation through uniform flow fields with the convected wave equations, for non-uniform flow fields it is required to solve the linearized Euler equations. On the other hand, non-linear wave propagations should be illustrated with the nonlinear Euler equations.

Acoustic problems arising from turbulent flow must be analysed with NS equations. The best approach to treat the problem is of course direct numerical simulation (DNS) of the turbulent flow field, where every scale of the eddies are taken into account. However, DNS of a realistic problem especially with high Reynolds numbers (containing much shorter waves) is computationally out of reach of current CPU capabilities due to super fine mesh domains requirement.

Instead, modelling the eddies rather than directly resolution is preferred to reduce the CPU cost. Reynolds-Averaged Navier-Stokes (RANS) simulation that models all the turbulent scales is one of the approaching methods. It takes the Reynolds time averaging of NS equations and since time average of each flow variable is kept constant, it brings the equations to steady form which is inadequate for solving unsteadiness of the turbulent flow. Although Unsteady RANS (URANS) equations are developed to remain the transient terms, RANS approach satisfies inaccurate results for the cases of large separations over a body where large eddies mostly exist [13, 32, 48]. The reason behind is that RANS attempts to model the large eddies with a universal model and since large eddies are influenced by the geometry of a body, they could not be simulated accurately with the universal models.

To overcome the drawback of RANS in massive separations, Large Eddy Simulation (LES) which resolves the large eddy structures directly and model the small ones has been introduced. LES takes a volume average of the equations instead of time averaging in RANS; in other words, LES applies a numerical grid filter. It makes sense to model only small, isotropic, homogeneous eddies which are more universal and resolve the others so that this kind of approach has been a remedy of the flow problems such as wake flow and large separation cases [13, 20]. However, using the grid volume filter could not reduce the CPU resources to feasible levels in the wall boundary layer for the problems that particularly involve the attached boundary layers.

To be able to defeat the disadvantages of both methods, Spalart et al. [57] have consequently introduced a new hybrid method of RANS and LES, named Detached Eddy Simulation (DES). This hybrid method which applies RANS near the solid boundary and LES far from the boundary provides not only an accurate solution through extensive problems but also less demand on computer usage. DES basically intents to model eddy viscosities in the boundary layer by RANS and then activates LES at the outer regions of the boundary layer to sort the detached eddies out in case of massive separation.

Even though DES reduces the fine grid requirement of LES in the boundary layer in general, it might have a problem during switching from RANS to LES mode with some doubtful grid types. In the event that parallel grid spacing to the wall is smaller than thickness of the boundary layer, LES mode is turned on in somewhere inside the boundary layer and not able to model all the velocity fluctuations accurately due to insufficient grid refinement there. Therefore, DES develops less eddy viscosity than it should be in the problem. This is called as Modelled-Stress Depletion (MSD) and to discard the dependency of grid spacings, Delayed Detached Eddy Simulation (DDES) has been presented as a modified version of DES by limiting the length scale with the eddy viscosity field [58].

Reynolds averaging of the NS equations has brought about new unknown terms, called Reynolds stresses and these extra unknowns could not be solved with the already governed equations (closure problem). First, Reynolds stress term has been described by an eddy viscosity through Boussinesq hypothesis. Then, to close the extra unknowns several models such as zero-equation (e.g. mixing length theory), one-equation (e.g. Spalart-Allmaras) and two-equation models (e.g. k-ω, k-ϵ) have being enhanced. By taking into consideration of experimental data Spalart-Allmaras one-equation turbulence model is more appropriate with the Detached Eddy Simulation [57].

1.6 CAA Applications for Wind Turbine Blade Sections

As stated before, the interaction of turbulent boundary layer with trailing edge of a blade constitutes the major component of modern wind turbine noise. Apart from some experimental and semi-theoretical studies exemplified in Chapter 1.3, many CAA applications with/without acoustic analogy have been carried on for aeroacoustic purposes around wind turbine blade sections. According to the study of Kamruzzaman et al. [32], it was emphasised that simulations with RANS be insufficient alone for detecting trailing edge noise. Although Ikeda et al. [28] achieved a noise radiation caused by low Reynolds number flow over a blade with DNS approach, it is not possible to perform a DNS study for high Reynolds number flow which is more realistic. Instead, LES has been preferred as one of the most common methods in blade simulations [20, 42].

Winkler [73] demonstrated the effect of a trailing edge blowing technique, which is for broadband noise reduction, over a blade section by LES simulation. Besides, Wolf and Lele [74] performed a successful trailing edge noise estimation study by LES for flow with high Reynolds number and low angle of attack around a wind turbine blade section with FW-H integral equation. A PhD study of Zhu [75] presented a similar work of both wind turbine blade section and whole turbine situations. However, as mentioned in Chapter 1.5, separation of boundary layers for large angle of attack flows could not be captured accurately by LES. Therefore, this affects a prediction of the trailing edge noise. This weakness of LES was demonstrated in the study of Ferreria [19]. Hence, wind turbine noise studies are being gone through hybrid LES-RANS, DES, and improvements of DES approaches.

Kim et al. [33] presented a noise simulation around a flatback airfoil with hybrid LES-RANS method. They achieved an adequate noise prediction generated by vortical flows leaving from a blunt trailing edge. Morris et al. [43] carried on a jet noise simulation study via DES approach based on SA one equation model, and they made noise prediction with FW-H integral equation. However, DES studies for aeroacoustic purposes around wind turbine blade sections have been recently conducted in literature.

1.7 The Objectives of The Thesis

The objective of the thesis is to develop a numerical solver that has a capability of turbulent flow simulations around wind turbine blade sections for aeroacoustic purposes. During the development, expected results to be achieved by the solver are summarised as follows:

- A high order accuracy,
- Adequate far field boundary conditions for minimum wave reflection,
- Accurate steady-state solutions for inviscid, viscous, and turbulent flow problems,
- Unsteady turbulent flow solutions of a wind turbine blade section for noise predictions.

1.8 The Scope of The Thesis

In the light of the information discussed up to now, for aeroacoustic purposes, a three dimensional, 4^{th} order, DRP, parallel, finite difference solver of NS equations and SA one equation model with DDES capability is developed in this thesis. A central differencing with an artificial dissipation is performed within the computational domain, and the far field boundary grid points are solved with the asymptotic solutions of the linearized Euler equations. In this thesis, the development process is mostly presented.

In Chapter 2, the methodology of this development is described. After the governing equations with the boundary conditions are given, spatial and temporal discretizations of the equations are explained. Then, implementations of the wall and far field boundary conditions are introduced. Finally, an artificial dissipation method to use is shown.

In Chapter 3, the results of various flow problems are presented. First, validation problems to demonstrate the order of accuracy, behaviour of far field equations, and implementations of inviscid, viscous, turbulent flux terms, and DDES to the solver are simulated. Then, an unsteady flow simulation is performed, and the results are discussed.

In Chapter 4, the conclusion of the thesis is presented with the comments and the future work.

CHAPTER 2

METHODOLOGY

2.1 Governing Flow Equations with Turbulence Model

As stated before, full, three dimensional, compressible, time-dependent Navier-Stokes equations are solved, in RANS form. In this chapter, first, these equations are given together with the turbulence model employed. Then, the numerical schemes used for solving these equations are described.

2.1.1 Compressible Reynolds-Averaged Navier-Stokes Equations

Three dimensional, unsteady, compressible RANS equations (also known as the Favre-averaged Navier-Stokes Equations) are given in Cartesian coordinates as:

$$\frac{\partial \mathbf{Q}}{\partial t} + \frac{\partial (\mathbf{E} - \mathbf{E}_v)}{\partial x} + \frac{\partial (\mathbf{F} - \mathbf{F}_v)}{\partial y} + \frac{\partial (\mathbf{G} - \mathbf{G}_v)}{\partial z} = 0 \tag{2.1}$$

where $\mathbf{Q}$ represents flow variables in vector form, and $(\mathbf{E}, \mathbf{F}, \mathbf{G})$ and $(\mathbf{E}, \mathbf{F}, \mathbf{G})_{vis}$ represent the inviscid and viscous flux vectors, respectively.

The conservative variables and the fluxes are given as:

$$
\begin{aligned}
\mathbf{Q} = \left\{ \begin{matrix} \bar{\rho} \\ \bar{\rho}\tilde{u} \\ \bar{\rho}\tilde{v} \\ \bar{\rho}\tilde{w} \\ \bar{\rho}\tilde{e}_t \end{matrix} \right\}, \mathbf{E} = \left\{ \begin{matrix} \bar{\rho}\tilde{u} \\ \bar{\rho}\tilde{u}^2 + \bar{p} \\ \bar{\rho}\tilde{u}\tilde{v} \\ \bar{\rho}\tilde{u}\tilde{w} \\ (\bar{\rho}\tilde{e}_t + \bar{p})\tilde{u} \end{matrix} \right\}, \mathbf{E_{vis}} &= \left\{ \begin{matrix} 0 \\ \bar{\tau}_{xx} \\ \bar{\tau}_{xy} \\ \bar{\tau}_{xz} \\ \bar{\tau}_{xx}\tilde{u} + \bar{\tau}_{xy}\tilde{v} + \bar{\tau}_{xz}\tilde{w} - \bar{q}_x \end{matrix} \right\}, \\
\mathbf{F} = \left\{ \begin{matrix} \bar{\rho}\tilde{v} \\ \bar{\rho}\tilde{v}\tilde{u} \\ \bar{\rho}\tilde{v}^2 + \bar{p} \\ \bar{\rho}\tilde{v}\tilde{w} \\ (\bar{\rho}\tilde{e}_t + \bar{p})v \end{matrix} \right\}, \mathbf{F_{vis}} &= \left\{ \begin{matrix} 0 \\ \bar{\tau}_{yx} \\ \bar{\tau}_{yy} \\ \bar{\tau}_{yz} \\ \bar{\tau}_{yx}\tilde{u} + \bar{\tau}_{yy}\tilde{v} + \bar{\tau}_{yz}\tilde{w} - \bar{q}_y \end{matrix} \right\}, \qquad (2.2) \\
\mathbf{G} = \left\{ \begin{matrix} \bar{\rho}\tilde{w} \\ \bar{\rho}\tilde{w}\tilde{u} \\ \bar{\rho}\tilde{w}\tilde{v} \\ \bar{\rho}\tilde{w}^2 + \bar{p} \\ (\bar{\rho}\tilde{e}_t + \bar{p})\tilde{w} \end{matrix} \right\}, \mathbf{G_{vis}} &= \left\{ \begin{matrix} 0 \\ \bar{\tau}_{zx} \\ \bar{\tau}_{zy} \\ \bar{\tau}_{zz} \\ \bar{\tau}_{zx}\tilde{u} + \bar{\tau}_{zy}\tilde{v} + \bar{\tau}_{zz}\tilde{w} - \bar{q}_z \end{matrix} \right\}
\end{aligned}
$$

where an overbar signifies Reynolds-averaging (or time-averaging), and a tilde signifies favre-averaging (or mass-averaging). If ϕ is defined as any instantaneous flow variable, Reynolds and favre averagings are represented separately as:

$$\bar{\phi} = \frac{1}{T}\int_T \phi dt \tag{2.3a}$$

$$\tilde{\phi} = \frac{\overline{\rho\phi}}{\bar{\rho}} \tag{2.3b}$$

where T represents a time interval.

The total energy term, $\tilde{e_t}$, is obtained as:

$$\tilde{e_t} = \frac{\bar{p}}{\bar{\rho}(\gamma - 1)} + \frac{1}{2}(\tilde{u}^2 + \tilde{v}^2 + \tilde{w}^2) \tag{2.4}$$

Shear stresses and heat flux terms including eddy viscosities (according to Boussinesq hypothesis) have the form as:

$$\bar{\tau}_{ik} = (\mu_{dyn} + \mu_{turb})\left[\left(\frac{\partial \tilde{u}_i}{\partial x_k} + \frac{\partial \tilde{u}_k}{\partial x_i}\right) - \frac{2}{3}\delta_{ik}\frac{\partial \tilde{u}_j}{\partial x_j}\right] \tag{2.5a}$$

$$\bar{q}_k = -\left(\frac{\mu_{dyn}}{Pr(\gamma - 1)} + \frac{\mu_{turb}}{Pr_t(\gamma - 1)}\right)\frac{\partial \tilde{T}}{\partial x_k} \tag{2.5b}$$

where $\tilde{u}_1 = \tilde{u}, \tilde{u}_2 = \tilde{v}, \tilde{u}_3 = \tilde{w}$ and $x_1 = x, x_2 = y, x_3 = z$. δ is the Kronecker delta. Extra unknown term μ_{turb} is calculated with Spalart-Allmaras (SA) turbulence model in order to close the flow equations.

2.1.2 Turbulence Modelling

The turbulent eddy viscosity, μ_{turb}, added to the molecular dynamic viscosity, μ_{dyn}, in Equation 2.5 is calculated by solving SA one equation model with Delayed Detached Eddy Simulation (DDES) approach. This is done simultaneously with the solution of NS equations.

2.1.2.1 Standard Spalart-Allmaras One Equation Model

The standard one equation model [56] is applied as in the following form (in non-conservation form and without trip term):

$$\frac{\partial \tilde{\nu}}{\partial t} + \mathbf{V} \cdot \nabla \tilde{\nu} = \Psi + \Pi - \Phi \tag{2.6}$$

where $\mathbf{V} = [\tilde{u}, \tilde{v}, \tilde{w}]$. Then, the turbulent eddy viscosity is obtained from;

$$\mu_{turb} = \rho f_{v1} \tilde{\nu} \tag{2.7}$$

The terms on the right hand side of Equation 2.6 represent diffusion, production and destruction, respectively. They are computed as:

$$\begin{gathered} \Psi = \nabla \cdot \left(\frac{\nu + \tilde{\nu}}{\sigma} \nabla \tilde{\nu} \right), \quad \Pi = c_{b1}(1 - f_{t2}) \tilde{S} \tilde{\nu} + \frac{c_{b2}}{\sigma} |\nabla \tilde{\nu}|^2, \\ \Phi = (c_{w1} f_w - \frac{c_{b1}}{\kappa^2} f_{t2}) \left[\frac{\tilde{\nu}}{d} \right]^2 \end{gathered} \tag{2.8}$$

where ν is the molecular kinematic viscosity. All variables shown in these expressions are calculated as:

$$\begin{gathered} f_{v1} = \frac{\chi^3}{\chi^3 + c_{v1}^3}, \quad \chi = \frac{\tilde{\nu}}{\nu}, \quad \nu = \frac{\mu_{dyn}}{\rho}, \quad \tilde{S} = S + \frac{\tilde{\nu}}{\kappa^2 d^2} f_{v2}, \\ f_{v2} = 1 - \frac{\chi}{1 + \chi f_{v1}} \quad f_w = g \left[\frac{1 + c_{w3}^6}{g^6 + c_{w3}^6} \right]^{1/6}, \\ g = r + c_{w2}(r^6 - r), \quad r = \min \left(\frac{\tilde{\nu}}{\tilde{S} \kappa^2 d^2}, r_{max} \right) \end{gathered} \tag{2.9}$$

where S is the vortex term computed as $S = |\nabla \times \mathbf{V}|$ and d is the distance to the nearest wall location. Parameters used in these equations are as follows:

$$\begin{aligned} \sigma = 2/3,\ c_{b1} = 0.1355,\ c_{b2} = 0.622,\ \kappa = 0.41,\ c_{w1} = \frac{c_{b1}}{\kappa^2} + \frac{1+c_{b2}}{\sigma}, \\ c_{w2} = 0.3,\ c_{w3} = 2,\ c_{v1} = 7.1,\ r_{max} = 10 \end{aligned} \tag{2.10}$$

2.1.2.2 Crivellini's Modification to the Spalart-Allmaras Model

It was suggested by Crivellini and D'Alessandro [12] that the standard SA model be basically modified through preventing calculation of fictitious source terms due to negative values of $\tilde{\nu}$. For this purpose, production and destruction terms $(\Pi - \Phi)$ were rearranged as in the following form:

$$\Pi - \Phi = \begin{cases} \left[(1-f_{t2})\frac{c_{b1}}{\kappa^2 r} - c_{w1} f_w + f_{t2}\frac{c_{b1}}{\kappa^2}\right]\left(\frac{\tilde{\nu}}{d}\right)^2 + \frac{c_{b2}}{\sigma}|\nabla\tilde{\nu}|^2, & \tilde{\nu} \geq 0 \\ 0, & \tilde{\nu} < 0 \end{cases} \tag{2.11}$$

The diffusion term, on the other hand, was modified as:

$$\Psi = \nabla \cdot \left(\frac{\nu + \max(\tilde{\nu}, 0)}{\sigma} \nabla \tilde{\nu} \right) \tag{2.12}$$

Moreover, the turbulent eddy viscosity was suggested to be computed as:

$$\mu_{turb} = \rho f_{v1} \max(\tilde{\nu}, 0) \tag{2.13}$$

Lastly, the function of r used in the source equation was given as:

$$r^* = \left(\frac{S\kappa^2 d^2}{\tilde{\nu}} + f_{v2} \right)^{-1} \tag{2.14a}$$

$$r = \begin{cases} r_{max}, & r^* < 0 \\ \min\left(r^*, r_{max}\right), & r^* \geq 0 \end{cases} \tag{2.14b}$$

The other functions and constants were kept the same as in the standard form. It was reported that with this modification a transition can be triggered in the laminar separation cases. However, it should be integrated differently for the attached flow circumstances. In this thesis, fully-turbulent flow is provided via DDES approach with the help of existence of initial eddy viscosity.

2.1.2.3 Implementation of Delayed Detached-Eddy Simulation

As mentioned before, DDES method is more appropriate to flow simulations involving separation and highly attached flow situations. Then DDES implementation, which simply switches the distance term nearest to the wall between RANS and LES modes with regard to less dependent on grid spacings, is done through [58]:

$$\tilde{d} = d - f_d \max(0, d - C_{DES}\Delta_{max}) \tag{2.15}$$

$$f_d = 1 - \tanh([8r_d]^3) \tag{2.16}$$

$$r_d = \frac{\nu_t + \nu}{(u_{i,j}u_{i,j})^{0.5}\kappa^2 d^2} \tag{2.17}$$

where $\Delta_{max} = \max(\mathit{\Delta} x, \mathit{\Delta} y, \mathit{\Delta} z)$, and the coefficient of $C_{DES} = 0.65$ which is determined based on a calibration to isotropic turbulence decay. Here, ν_t represents the turbulent kinematic viscosity and $u_{i,j}$ represents the velocity gradient ($\frac{\partial u_i}{\partial x_j}$).

Although there are some further improvements to this mode (Zonal DES [14], and Extended DDES [52]) to prevent possible instabilities of switching between the modes (named as a gray area problem), it has not been proven yet that their applications are really needful. Therefore, DDES mode has been decided to use in this study.

2.2 Boundary Conditions

The governing equations are solved with the physical information of conservative flow variables at computational boundaries in the view of the aeroacoustic purposes. In this section, wall and far field boundary conditions are described, respectively.

2.2.1 Wall Boundary Conditions

The wall boundary (surface of the body) conditions are applied according to the following physical information:

Inviscid wall boundary conditions:

- *Velocity*: Normal velocity component to the wall is zero ($\mathbf{V} \cdot \tilde{n} = 0$). Other components are found by extrapolations.

- *Pressure*: Normal derivative of pressure is obtained from the momentum equation parallel to the wall ($\nabla p \cdot \tilde{n} = -p\tilde{n} \cdot ((\mathbf{V} \cdot \nabla)\mathbf{V})$).
- *Density*: Total enthalpy is preserved ($h_\infty = h_{local} = \frac{\gamma p}{\rho(\gamma-1)} + \frac{1}{2}\rho|\mathbf{V}|^2$).

Viscous wall boundary conditions:

- *Velocity*: All velocity components on the wall are zero due to the no-slip condition ($\mathbf{V} = 0$).
- *Pressure*: Normal derivative of pressure is zero ($\nabla p \cdot \tilde{n} = 0$).
- *Density*: For adiabatic cases, normal derivative of density is zero ($\nabla \rho \cdot \tilde{n} = 0$). However, for non-adiabatic cases, it is obtained from the equation of state ($p = \rho RT$).

Finally, the turbulent eddy viscosity term is taken as zero on the wall point since there is no turbulence there.

2.2.2 Far Field Boundary Conditions

In acoustic problems, the waves created by the source should go out of the computational domain with a negligible reflection. Therefore, far field conditions should be constructed in considerations of the propagation characteristics of each waves.

Outgoing waves are classified according to their characteristics as entropy, acoustic, and vorticity waves. Tam and Webb showed that the asymptotic solutions of the linearized Euler equations contain these characteristics waves [64]. Accordingly, far field boundary conditions are represented by two different set of equations which are radiation and outflow equations. While the radiation boundary conditions are related to the acoustic disturbances only, the outflow boundary conditions involve the combination of all disturbances of entropy, acoustic, and vorticity waves. If a disturbance to a quantity q is defined as $q' = q - q_\infty$, then 3 dimensional radiation boundary condition equations in polar coordinates are given as:

$$\frac{\partial}{\partial t}\begin{Bmatrix}\rho'\\ \mathbf{V}'\\ p'\end{Bmatrix}+V(\theta)\left(\frac{\partial}{\partial r}+\frac{1}{r}\right)\begin{Bmatrix}\rho'\\ \mathbf{V}'\\ p'\end{Bmatrix} \tag{2.18}$$

3 dimensional outflow boundary condition equations are as follows:

$$\frac{\partial \rho'}{\partial t}+\mathbf{V}_\infty\cdot\nabla\rho'=\frac{1}{(c_\infty)^2}\left(\frac{\partial p'}{\partial t}+\mathbf{V}_\infty\cdot\nabla p'\right) \tag{2.19a}$$

$$\frac{\partial \mathbf{V}'}{\partial t}+\mathbf{V}_\infty\cdot(\nabla\mathbf{V}')=-\frac{1}{\rho_\infty}\nabla p' \tag{2.19b}$$

$$\frac{\partial p'}{\partial t}+V(\theta)\left(\frac{\partial}{\partial r}+\frac{1}{r}\right)p'=0 \tag{2.19c}$$

where $V(\theta)$ is given by;

$$V(\theta)=\mathbf{V}\cdot\hat{e_r}+\left(a^2-(\mathbf{V}\cdot\hat{e_\theta})^2\right)^{1/2} \tag{2.20}$$

r is taken as the radial distance from the source location to the far field boundary points. However, the question here is which point in the domain should be taken as the source location? To compensate this confusion, if the far field boundary is composed sufficiently far from the body, the term $1/r$ in the asymptotic equations will not change from one reference point to another taken within the domain.

Bogey and Bailly demonstrated that using the linearized Euler equations at far field grid nodes together with NS equations at interior domains does not damage the simulation process at all; on the contrary, it serves as a non-reflecting artificial boundary as intended [5].

Furthermore, the far field condition of the turbulent eddy viscosity term is generally selected as $\tilde{\nu}_{farfield}=3\nu_\infty$ to $5\nu_\infty$ in order to provide a turbulent flow field continuously to the computational domain [59].

2.2.3 RANS Equations Transformed to Computational Domains

Discretizations of the governing equations are conducted within the computational domain. Therefore, the equations are transformed from the physical domain to the computational domain. The transformed version of compressible RANS equations given in a flux vector form in Equation 2.1 are as follows:

$$\frac{\partial \hat{\mathbf{Q}}}{\partial \tau} + \frac{\partial (\hat{\mathbf{E}} - \hat{\mathbf{E}}_v)}{\partial \xi} + \frac{\partial (\hat{\mathbf{F}} - \hat{\mathbf{F}}_v)}{\partial \eta} + \frac{\partial (\hat{\mathbf{G}} - \hat{\mathbf{G}}_v)}{\partial \zeta} = 0 \tag{2.21}$$

where τ, ξ, η, and ζ represent time and space coordinates of the computational domain. Each flux term is calculated with Jacobian terms as:

$$\hat{\mathbf{Q}} = \frac{\mathbf{Q}}{J} \tag{2.22a}$$

$$\hat{\mathbf{E}} = \frac{1}{J} \left(\xi_t \mathbf{Q} + \xi_x \mathbf{E} + \xi_y \mathbf{F} + \xi_z \mathbf{G} \right) \tag{2.22b}$$

$$\hat{\mathbf{F}} = \frac{1}{J} \left(\eta_t \mathbf{Q} + \eta_x \mathbf{E} + \eta_y \mathbf{F} + \eta_z \mathbf{G} \right) \tag{2.22c}$$

$$\hat{\mathbf{G}} = \frac{1}{J} \left(\zeta_t \mathbf{Q} + \zeta_x \mathbf{E} + \zeta_y \mathbf{F} + \zeta_z \mathbf{G} \right) \tag{2.22d}$$

2.3 Discretizations of the Equations

The idea of high order DRP discretizations, suggested by Tam and Webb [64], is based on minimizing the dispersion error of discrete forms of derivatives in the governed equations. In order to determine the discretization coefficients of the DRP scheme they proposed a procedure as follows: Firstly, a transformed wavenumber/angular frequency is obtained from Fourier/Laplace transforms of the governing differential equations. Then, the optimized (DRP) coefficients which minimize the dispersion error caused by a difference between the transformed and actual wavenumbers/angular frequencies are obtained. In this section, a 4^{th} order DRP numerical discretizations of the parallel, explicit, finite difference solver, developed to solve the 6 partial differential equations which are equations of continuity, 3 momentum, energy, and SA one equation model, are described in space and time domains.

2.3.1 Spatial Discretization

The classical 4^{th} order finite difference scheme is satisfied with 5 grid nodes. However, to provide DRP feature one extra coefficient, as a free parameter, is used for the optimization. After this coefficient is found, other coefficients are easily calculated by classical Taylor series approach. Therefore, with the addition of this extra coefficient spatial derivatives of the equations are discretized with 7 nodes to reach 4^{th} order accurate DRP scheme. For the nodes in the interior region of computational domains, central differencing is applied. However, at boundary regions where the number of nodes are limited, backward/forward discretizations are applied. In Figure 2.1, while point A represents the central differencing, point *B* represents the backward/forward differencing.

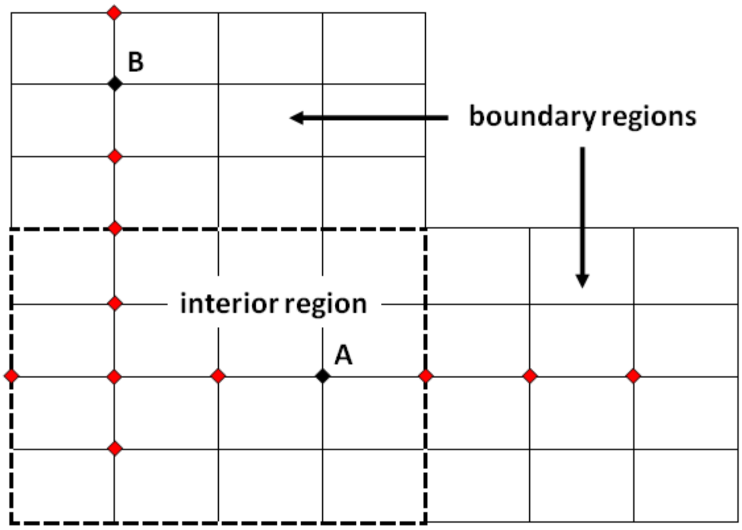

Figure 2.1: Spatial discretizations at inner and boundary regions of the computational domain

The weights of the central DRP scheme were obtained by Tam and Webb [64] as follows:

First, any partial differential term of an l^{th} node in a uniform grid was expanded with the finite difference approximation by 7 nodes as:

$$\left(\frac{\partial f}{\partial x}\right)_l \simeq \frac{1}{\Delta x}\sum_{j=-3}^{3} a_j f_{l+j} \tag{2.23}$$

Here, the parameters of a_j are the DRP coefficients. When Fourier transform was applied to left and right hand sides of Equation 2.23 as:

$$\widetilde{f}(\alpha) = \frac{1}{2\Pi} \int_{-\infty}^{\infty} f(x) e^{-i\alpha x} dx, \tag{2.24}$$

a transformed wavenumber, $\widetilde{\alpha}$, was found as follows:

$$\widetilde{\alpha} = \frac{-i}{\Delta x} \sum_{j=-3}^{3} a_j e^{ij\alpha\Delta x} \tag{2.25}$$

The phase of the transformed wave, $\widetilde{\alpha}\Delta x$, is actually a periodic function of the phase of the differential term, $\alpha\Delta x$, with period of 2π. On the other hand, any sinusoidal wave can be defined with at least 5 grid points in computational domains. This means that its wavelength should be equal or bigger than 4 grid spacings. In other words, the phase of the wave should be smaller than $\pi/2$. Therefore, the dispersion error between the actual and transformed phase was defined in the range of $\pi/2$ as:

$$E = \int_{-\pi/2}^{\pi/2} |\alpha\Delta x - \widetilde{\alpha}\Delta x|^2 d(\alpha\Delta x) \tag{2.26}$$

The spatial discretization coefficients that satisfy the condition of minimization of this error,

$$\frac{\partial E}{\partial a_j} = 0, \tag{2.27}$$

were finally derived. Governed DRP coeficients to be used in central spatial discretizations are as follows:

$$\begin{aligned} a_{j=0} = & \quad 0, \\ a_{j=1} = & \ -a_{j=-1} = \ 0.79926643, \\ a_{j=2} = & \ -a_{j=-2} = \ -0.189413314, \\ a_{j=3} = & \ -a_{j=-3} = \ 0.02651995 \end{aligned}$$

In case of a requirement of backward/forward discretizations at boundaries, Tam and Dong gave DRP coefficients for all possible non-central schemes [62] as:

$$\begin{aligned} a_{(j=4 \ to \ j=-2)} &= [0.049041958, -0.468840357, -0.474760914, 1.273274737, \\ &\quad -0.518484526, 0.166138533, -0.026369431], \\ a_{(j=4 \ to \ j=-2)} &= [-0.209337622, -1.084875676, 2.14777605, -1.388928322, \\ &\quad 0.768949766, -0.28181465, 0.048230454], \\ a_{(j=4 \ to \ j=-2)} &= [-2.192280339, 4.748611401, -5.108851915, 4.461567104, \\ &\quad -2.833498741, 1.128328861, -0.203876371] \end{aligned}$$

To see the superiority of the DRP scheme to the standard one, the dispersion relations obtained by different numerical schemes are compared. Figure 2.2 shows the comparison of $\alpha\Delta x$ of a first derivative of a function with $\widetilde{\alpha}\Delta x$. Appendix A gives the details of the formulations of dispersion relations obtained by different numerical schemes.

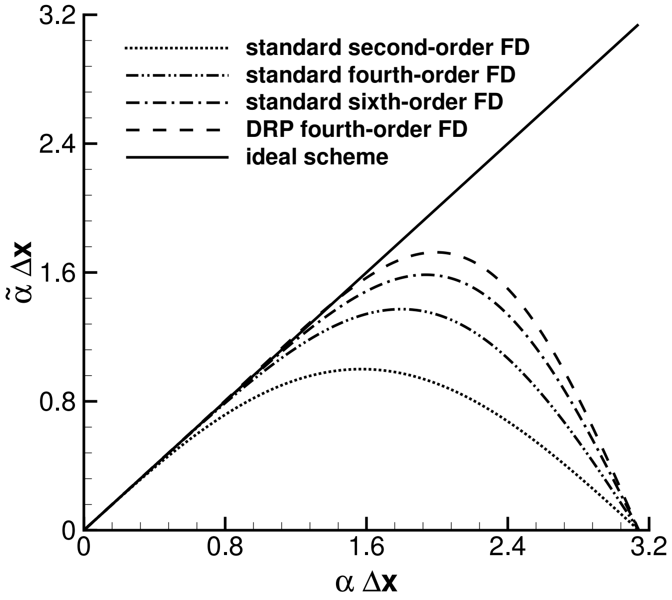

Figure 2.2: Comparison of the wavelengths resolved by different numerical schemes with one mesh spacing

As seen in Figure 2.2, one mesh spacing can resolve 1.45 radian part of the whole phase with fourth-order DRP scheme. This means that for accurate wave resolution approximately $(2\pi/1.4 \backsimeq)$ 4.5 mesh spacings at least are required. In other respects, standard sixth-order, fourth-order and second-order schemes need 6.3, 9 and 15.7 mesh spacings, respectively. Therefore, this study shows that high-order DRP numerical methods are more prone to simulate physical waves with equivalent computational domains than low-order or standard numerical methods.

2.3.2 Temporal Discretization

Temporal derivatives of the governing equations are discretized with DRP Linear Multistep (LM) method which was suggested by Tam and Webb [64] due to its low dissipation and low dispersion features. However, in steady-state simulations of this thesis compact four-stage Runge-Kutta (RK4) method [30] is preferred since it converges to steady solutions with higher CFL numbers than the LM method.

2.3.2.1 Linear Multistep scheme with DRP

The LM discretization method with 4^{th} order DRP scheme was developed by Tam and Webb with the same approach used in the spatial discretizations as following steps:

First, any time derivative term at n^{th} time step was expanded with Taylor series by 4 time steps as follows:

$$Q^{n+1} - Q^{n} \simeq \Delta t \sum_{j=0}^{3} b_j \left(\frac{dQ}{dt} \right)^{n-j} \tag{2.28}$$

The transformed angular frequency of Equation 2.28 applied Laplace transform was found as:

$$\widetilde{\omega} = \frac{i(e^{-i\omega\Delta t} - 1)}{\Delta t \sum_{j=0}^{3} b_j e^{ij\omega\Delta t}} \tag{2.29}$$

DRP coefficients of the temporal discretizations obtained from minimizing the error between the actual angular frequency of the differential term and the transformed one are given as:

$$\begin{aligned}
b_{j=0} &= \quad 2.30255809, \\
b_{j=1} &= -2.49100760, \\
b_{j=2} &= \quad 1.57434093, \\
b_{j=3} &= -0.38589142
\end{aligned}$$

The discretization algorithm of the 3D, explicit, 4^{th} order, DRP finite difference solver in Cartesian coordinates (for inner regions of the computational domain) is as follows:

The flux vector, $\mathbf{A}$, obtained from spatial discretization is given as:

$$\begin{aligned}\mathbf{A}(x,y,z,t) = &-\frac{1}{\Delta x}\sum_{j=-3}^{3} a_j\mathbf{E}(x+j\Delta x,y,z,t) - \frac{1}{\Delta y}\sum_{j=-3}^{3} a_j\mathbf{F}(x,y+j\Delta y,z,t) \\ &-\frac{1}{\Delta z}\sum_{j=-3}^{3} a_j\mathbf{G}(x,y,z+j\Delta z,t)\end{aligned} \tag{2.30}$$

The conservative flow variable vector, $\mathbf{Q}$, after one time step, Δt, obtained from temporal discretization is given as:

$$\mathbf{Q}(x,y,z,t+\Delta t) = \mathbf{Q}(x,y,z,t) + \Delta t\sum_{j=0}^{3} b_j\mathbf{A}(x,y,z,t-j\Delta t) \tag{2.31}$$

The discretization algorithm can also be written in computational domains as follows:

$$\begin{aligned}\mathbf{A}(\xi,\eta,\zeta,\tau) = &-\sum_{j=-3}^{3} a_j\hat{\mathbf{E}}(\xi+j,\eta,\zeta,\tau) - \sum_{j=-3}^{3} a_j\hat{\mathbf{F}}(\xi,\eta+j,\zeta,\tau) \\ &-\sum_{j=-3}^{3} a_j\hat{\mathbf{G}}(\xi,\eta,\zeta+j,\tau)\end{aligned} \tag{2.32}$$

$$\hat{\mathbf{Q}}(\xi,\eta,\zeta,\tau+1) = \hat{\mathbf{Q}}(\xi,\eta,\zeta,\tau) + \sum_{j=0}^{3} b_j\mathbf{A}(\xi,\eta,\zeta,\tau-j) \tag{2.33}$$

where $\hat{\mathbf{Q}}$, $\hat{\mathbf{E}}$, $\hat{\mathbf{F}}$, and $\hat{\mathbf{G}}$ are computed from Equation 2.22.

2.3.2.2 Compact four-stage Runge-Kutta scheme

The compact RK4 temporal discretization scheme after getting the flux terms, $\mathbf{A}$, with DRP method as in LM integration is given as:

$$\begin{aligned} q^{(0)} &= \mathbf{Q}(x,y,z,t) \\ q^{(1)} &= q^{(0)} - \beta_1\Delta t\mathbf{A}(q^{(0)}) \\ q^{(2)} &= q^{(0)} - \beta_2\Delta t\mathbf{A}(q^{(1)}) \\ q^{(3)} &= q^{(0)} - \beta_3\Delta t\mathbf{A}(q^{(2)}) \\ \mathbf{Q}(x,y,z,t+\Delta t) &= q^{(0)} - \beta_4\Delta t\mathbf{A}(q^{(3)}) \end{aligned} \tag{2.34}$$

where the coefficients are: $\beta_1 = 1/4$, $\beta_2 = 1/3$, $\beta_3 = 1/2$, $\beta_1 = 1$.

2.3.2.3 Implementation of The Boundary Conditions

Maintaining the use of the central discretization schemes within the computational domain is important for low dissipation. However, this could be possible at boundary regions with only existence of extra three ghost nodes that are not in the physical domain. On the other hand, damping out the spurious short waves created by the high-order discretizations of the partial differential equations is another remarkable point. Therefore, the boundary conditions are constructed with these considerations.

Tam and Dong proposed that there should be one ghost grid node created inside the wall for each boundary grid nodes. However, the number of ghost values should be selected as much as the number of defined equations due to physical requirements on the wall. Then, normal derivatives of the variables that cause these requirements should be discretized by non-central DRP schemes with the help of their ghost values [62]. To illustrate, for 2 dimensional viscous flow problems there must be no-slip condition that enforces zero velocity on the wall ($u_{wall} = 0, v_{wall} = 0$), and the pressure and shear stress variables (p, τ_{xy}) are responsible for zero velocity. Therefore, while these variables are discretized in the perpendicular direction to the wall with their ghost values (like point A in Figure 2.3), all the remaining variables are discretized with only their interior points (like point B in Figure 2.3).

For the linearized equations, the use of the non-central schemes at boundaries can damp out the numerical contamination due to spurious short waves; however, when non-linearized equations are the point in question, this methodology becomes complicated and may cause numerical instabilities [61]. As an ideal way in this thesis, it is decided to maintain the central schemes with the addition of an artificial dissipation to clean the unwanted short waves (see Chapter 2.4). Therefore, three ghost grid points for each wall points and each flow variables need to be defined. The ghost values of velocity components, density, pressure, and turbulent eddy viscosity terms are obtained by extrapolations according to Dirichlet and Neumann type conditions with respect to the wall boundary conditions given in Chapter 2.2.1. Then, the ghost values of total energy term are directly calculated with the ghost values of other variables (see Equation 2.4).

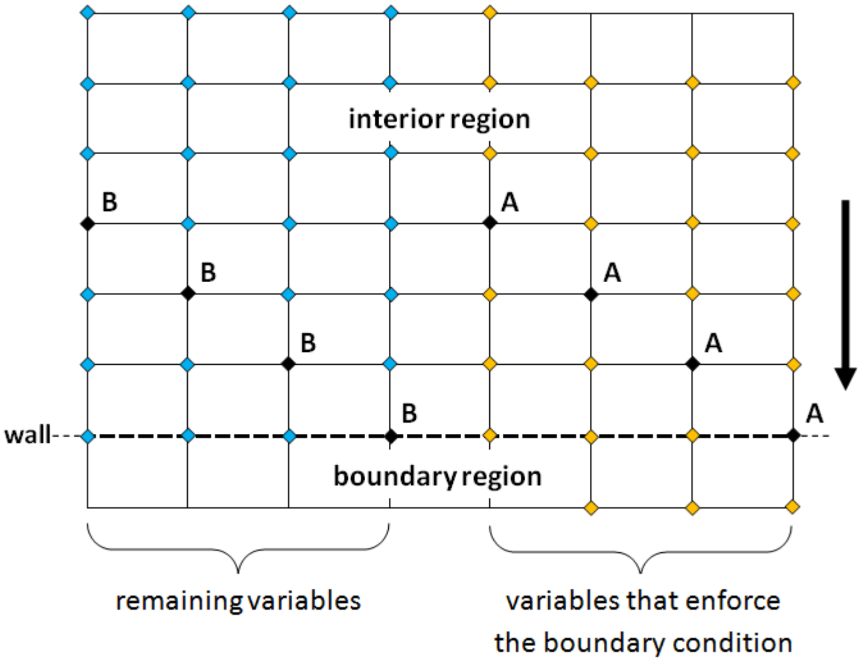

Figure 2.3: An alternative to spatial discretizations near the wall boundary

On the other hand, since the linearized Euler equations are used instead of the nonlinear NS equations at the far field boundary, it is preferred to use a backward finite differencing for three ghost nodes at outer boundary (like point B in Figure 2.1) with the help of the non-central DRP coefficients.

2.4 Artificial Dissipation

High-order discretizations of the partial differential equations cause contamination with spurious short waves that cannot be simulated exactly due to different propagation characteristics from those of large waves. Therefore, an artificial dissipation is added to the governing equations to clean up the contamination. In this section, the artificial dissipation method applied to the developed solver is described after introducing some other methods.

Since the high-order DRP algorithm of Tam and Webb is used in this thesis, the artificial dissipation method recommended by them [65] has been firstly intended to use. For any l^{th} point in the computational domain, the artificial dissipation term is added to the governing equations as:

$$\frac{\partial \hat{\mathbf{Q}}_l}{\partial \tau} + \frac{\partial (\hat{\mathbf{E}} - \hat{\mathbf{E}}_v)_l}{\partial \xi} + \frac{\partial (\hat{\mathbf{F}} - \hat{\mathbf{F}}_v)_l}{\partial \eta} + \frac{\partial (\hat{\mathbf{G}} - \hat{\mathbf{G}}_v)_l}{\partial \zeta} = -\mu_{ad} \sum_{j=-3}^{3} c_j \hat{\mathbf{Q}}_{l+j} \tag{2.35}$$

where μ_{ad} is the weight of the artificial dissipation term, and it is taken as constant for all nodes in the domain.

Although this algorithm damps the spurious waves out sufficiently in inviscid flow problems, it cannot show this achievement in viscous flow problems where high gradients of flow variables and variational mesh densities take place. The reason is that this algorithm cannot adapt itself to these changes. To compensate this, Tam and Shen proposed a selective artificial dissipation algorithm [63] which is changing with the flow conditions. However, it may cause a numerical instability feature in more complicated flow problems due to its non-conservative form.

Lastly, the artificial dissipation model introduced by Jameson, Schmidt and Turkel (named as JST model) [31] that is both conservative and adjusted itself to different flow conditions has settled the matter. This model is, in origin, appropriate to the 2^{nd} order algorithms. Cengiz raised the order of the artificial dissipation accuracy to the 4^{th} order by the 6^{th} order differencing terms [8].

For 3 dimensional, 4^{th} order accurate algorithms, JST type artificial dissipation terms which are added to the right hand side of the flow equations are given in the computational domain (for any l^{th} point) as follows:

$$\frac{\partial \hat{\mathbf{Q}}_l}{\partial \tau} + \frac{\partial (\hat{\mathbf{E}} - \hat{\mathbf{E}}_v)_l}{\partial \xi} + \frac{\partial (\hat{\mathbf{F}} - \hat{\mathbf{F}}_v)_l}{\partial \eta} + \frac{\partial (\hat{\mathbf{G}} - \hat{\mathbf{G}}_v)_l}{\partial \zeta} = \mathcal{L}_{AD} \hat{\mathbf{Q}}_l \tag{2.36}$$

$$\mathcal{L}_{AD} \hat{\mathbf{Q}}_l = (D_\xi^2 + D_\eta^2 + D_\zeta^2 + D_\xi^6 + D_\eta^6 + D_\zeta^6) \hat{\mathbf{Q}}_l \tag{2.37}$$

The 2^{nd} and 6^{th} order terms are defined as:

$$D_\xi^2 \hat{\mathbf{Q}}_l = \nabla_\xi \left[\lambda_l \epsilon_l^{(2)} \Delta_\xi \right] \hat{\mathbf{Q}}_l \tag{2.38a}$$

$$D_\xi^6 \hat{\mathbf{Q}}_l = \nabla_\xi \Delta_\xi \nabla_\xi \left[\lambda_l \epsilon_l^{(6)} \Delta_\xi \nabla_\xi \Delta_\xi \right] \hat{\mathbf{Q}}_l \tag{2.38b}$$

where ∇_ξ and Δ_ξ represent the forward and backward differencing schemes, respectively. $\epsilon^{(6)}$ is the weight of the artificial dissipation term, and λ represents the spectral radius. Here, the 2^{nd} order terms are necessary for transonic flows to capture the shock. $\epsilon^{(2)}$ behaves like a pressure sensor and calculated as:

$$\epsilon_l^{(2)} = min(20s_{JST}^2, s_{JST}) \tag{2.39}$$

where s_{JST} is the pressure sensor term:

$$s_{JST} = \frac{|\tilde{p}_{\xi+1,\eta,\zeta} - 2\tilde{p}_{\xi,\eta,\zeta} + \tilde{p}_{\xi-1,\eta,\zeta}|}{\tilde{p}_{\xi+1,\eta,\zeta} + 2\tilde{p}_{\xi,\eta,\zeta} + \tilde{p}_{\xi-1,\eta,\zeta}} \tag{2.40}$$

Therefore, JST type artificial dissipation model adapted to the 4^{th} order accurate algorithms by Cengiz [8] is decided to use in the developed solver to damp out the spurious short waves.

2.5 Ffowcs Williams-Hawkings Equation

It is expensive to directly simulate the sound radiated to the far away regions by numerical discretizations. Thus, FW-H integral equation is solved with the data of flow variables resolved near the source body. In this section, FW-H integral equation and its implementation to the solver are presented.

General FW-H equation [72] composed as a wave equation after rearranging NS equations is as follows:

$$\left(\frac{\partial^2}{\partial t^2} - c_0^2\frac{\partial^2}{\partial x_i \partial x_i}\right)(H(f)\rho') = \frac{\partial^2}{\partial x_i \partial x_i}(T_{ij}H(f)) - \frac{\partial}{\partial x_i}(F_i\delta(f)) + \frac{\partial}{\partial t}(Q\delta(f)) \tag{2.41}$$

where $f = 0$ represents FW-H surface, a subscript of 0 denotes the values far from the surface, and a prime ($'$) denotes the perturbation values. H is Heaviside and δ is Dirac delta function. For 3D flow, i is taken as 1, 2, and 3. Moreover, $T_{i,j}$, F_i and Q represent quadrupole, dipole and monopole source terms, respectively. Here are the formulations of the source terms:

$$T_{ij} = \rho u_i u_j + p\delta_{ij} - c_0^2\rho'\delta_{ij} \tag{2.42}$$

$$F_i = (p\delta_{ij} + \rho(u_i - 2U_i)u_j + \rho_0 U_i U_j)\frac{\partial f}{\partial y_j} \tag{2.43}$$

$$Q = (\rho u_i - \rho_0 U_i)\frac{\partial f}{\partial y_i} \tag{2.44}$$

In the above equations, while u is the local flow velocity, $-U$ represents FW-H surface velocity. δ_{ij} is again Kronecker delta. Furthermore, $\partial f/\partial y$ terms represent the normal derivatives of the integral surface.

A time-domain or frequency-domain solution of Equation 2.41 was obtained from the implementation of Green function via wave equation operator. 3D time-domain solution was formulated efficiently by Farassat [17]. On the other hand, 2D and 3D frequency-domain solutions were demonstrated in Lockard's studies [38, 39].

In order to detect the waves with certain frequencies that could be resolved in the range of the capability of the solver, 3D frequency-domain FW-H solution is used in this thesis. The final equation that gives the perturbation density values at the observer location is as follows (in the form of [39]):

$$\begin{aligned} H(f)c_0^2\rho'(\mathbf{y},\omega) = &- \int_{f>0} T_{ij}(\xi,\omega)H(f)\frac{\partial^2 G(\mathbf{y};\xi)}{\partial\xi_i\partial\xi_j}d\xi \\ &- \oint_{f=0} F_i(\xi,\omega)\frac{\partial G(\mathbf{y};\xi)}{\partial\xi_i}dl \\ &- \oint_{f=0} i\omega Q(\xi,\omega)G(\mathbf{y};\xi)dl \end{aligned} \tag{2.45}$$

where $\mathbf{y}$ and ξ denote the observer and source coordinates in vector forms, respectively. Green function for a wave equation is given for the flow in y_1 direction as:

$$G(\mathbf{y};\xi) = \frac{-1}{4\pi d}e^{-ik(d-M(y_1-\xi_1))/\beta^2} \tag{2.46}$$

where d is a distance which is equal to $\sqrt{(y_1-\xi_1)^2+\beta^2(y_2-\xi_2)^2+\beta^2(y_3-\xi_3)^2}$, i is complex number, M is Mach number, k is wavenumber (ω/c_o), and β is Prandtl-Glauert factor ($\sqrt{1-M^2}$).

Each terms in Equation 2.45 are integrated by summation of all the values of each grids in the identified regions. That is to say that while monopole and dipole source terms are integrated along FW-H surface area, quadrupole source terms are integrated along a volume out of FW-H surface.

Integral surface of FW-H equation can be selected as both the surface of the body and a near field surface (called as the permeable surface). If the permeable surface is constituted including all the turbulent regions that cause noise, it is not needed to make quadrupole volume integrations so that the contributions of the surface integrals alone would be enough.

2.6 Development of the Solver

The commercial CFD programs do not have enough numerical capability of simulating aeroacoustic problems because of their low order numerical accuracy. This is why a CAA solver is required to be developed with the purpose of noise estimation of wind turbine blade sections. In this section, firstly, the coding language of the solver is introduced. Then, how the solver is parallelized is described. Finally, a parallel speedup graph obtained by multiple cores in a high performance cluster is demonstrated.

2.6.1 Coding Language

The solver is coded via Fortran programming language. Fortran 90 which is one of the newest versions is preferred to use. The reasons of the decision are summed up in Table 2.1 through conspicuous features unavailable in the oldest versions:

Feature	**Intended Purpose**
Module	group data together and make them available when necessary
Allocate-Deallocate	allow a dynamic memory allocation when necessary
Pointer	create dynamic data structures without allocate extra memory
Select-Case	make multiple selection faster instead of using *if* loop

Table 2.1: Programming features that come with the version of Fortran 90

The newer versions such as Fortran 2003/2008/2015 have renewals mostly in the area of object-oriented programming. Therefore, Fortran 90 is decided to be adequate to develop the desired solver in an efficient way. Moreover, *double precision* is used during programming the solver to minimize the round-up errors.

2.6.2 Parallelization Procedure

Since much fine stencil sizes are required to simulate the large frequency acoustic waves and much more time iterations are needed to converge to solutions with high-order methods during the simulations, computation cost becomes huge when the equations are solved with a sequential code. This brings the necessity of making the solver parallel meaning that the code works with multi-processors.

There are two commonly-used multi-processing language: OpenMP and Open MPI. Although the implementation of the functions of OpenMP is easier than those of Open MPI, OpenMP only provides a communication between the cores in a single node. Open MPI, on the other hand, can supply a communication between several nodes and this gives an advantage to be able to use more processors. In addition to that, the linear speedup can be easily preserved with increasing the number of processors with Open MPI; however, OpenMP does not guarantee the speedup. Thus, Open MPI functions are preferred to implement into the solver to make it parallel.

After all processors are initialized and ranked with simple Open MPI functions, equalized computational domains are distributed to them. Therefore, each processors start to solve all the flow equations in their local domains. In every iteration after solving the internal domain numerically, the global boundary values are identified. This procedure is exactly the same as in the sequential code. However, there are also boundary values of local domains of the processors to be determined. Therefore, these values are taken from the internal domain of neighbour processors by communication. Remind from Chapter 2.2.1, it is told that three ghost nodes are used to preserve the central scheme. During the communication between the processors in neighbourhood relations, three ghost nodes are transferred in each axis direction. Figure 2.4 represents the communication process in i direction.

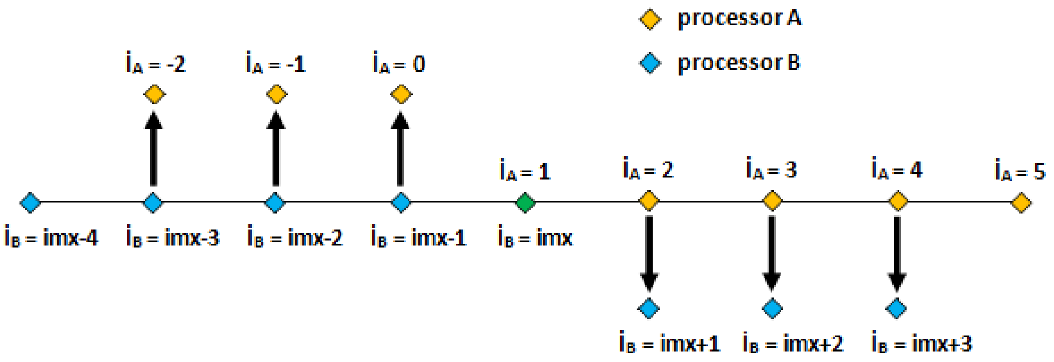

Figure 2.4: Communication between processors for local boundary values

All multi-processing simulations of this thesis are done in METUWIND (METU Center for Wind Energy) HPC cluster that has 8 nodes and 512 cores. The speedup test that demonstrates how the speed of the solver increases with the number of processors is done to see the efficiency of the solver. The result of the speedup test up to 64 cores is shown in Figure 2.5.

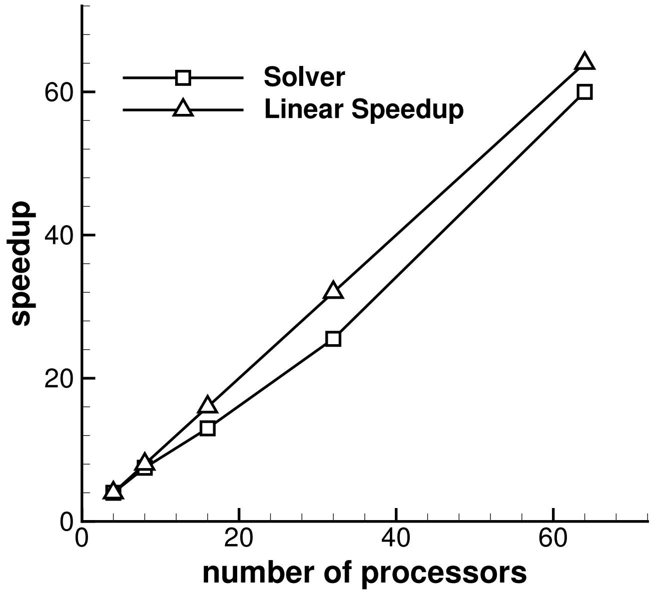

Figure 2.5: Comparison of the speedup of the solver with the linear speedup curve

The reason of a deviation from the linear speedup line is that the communication process might slow down the simulations. Nevertheless, multi-processing efficiency of the solver is good enough for long duration simulations.

CHAPTER 3

RESULTS AND DISCUSSION

As aforementioned, high order methods have lower dispersion and dissipation errors. Keeping them at acceptable levels is important for unsteady simulations. Therefore, before starting to solve unsteady problems, order of accuracy of the developed solver, which is desired to be 4^{th} order, is demonstrated firstly. Then, far field reflection testing is done to see the outgoing ability of acoustic waves from computational domains without significant reflections. After that, inviscid and viscous flux computations of the solver are tested with some steady-state problems that have analytical solutions or solutions validated with experimental studies in literature. With these problems, it is aimed to see the artificial dissipation effects on the solver as well. Then, implementation of DDES algorithm is validated with a 'severe' grid problem. Finally, an unsteady problem over a wind turbine blade section (NACA0012) is introduced and turbulent flow results obtained from unsteady simulations are demonstrated with the comparisons and comments. Note that flow directions of the problems including convection are selected through the positive coordinate systems.

3.1 Testing of Order of Accuracy

It is suitable to simulate a convection problem of an isentropic vortex in order to check the order of accuracy of the solver. The problem simply includes a 2D convection simulation of an isentropic vortex. The simulation is done with inviscid (Euler) equations with periodic boundary conditions and without artificial dissipation. Since this is a pure convection inviscid flow problem, all flow characteristics of the vortex is expected to be preserved during convection.

In the simulation, the vortex is convected through 3 different non-uniform Cartesian meshes that have 50×50, 100×100 and 200×200 grid points, separately. Each non-uniform mesh is created with sine and cosine functions. It is expected that 4^{th} order of accuracy is provided with the change of the grid sizes. On the other hand, the reason of the use of non-uniform meshes is to show that the order of accuracy does not depend on the mesh uniformity. Time step of all mesh domains is selected with respect to the fines one. The reason is that time step is calculated with respect to the smallest grid spacing in unsteady simulations as well.

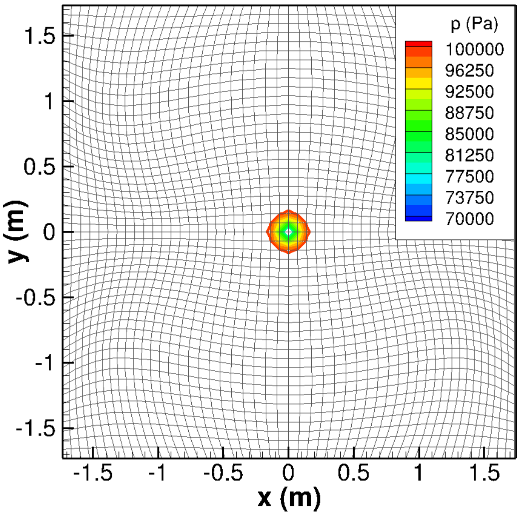

Figure 3.1: Initial pressure contours of the isentropic vortex on a non-uniform mesh

The vortex is convected with the speed of $V_\infty = 200$m/s. Initial conditions of the vortex are given in the following formulations which are created by Gaussian distribution as follows:

$$\mathbf{V} = \begin{Bmatrix} V_\infty \\ 0 \\ 0 \end{Bmatrix} + u_A e^{(1-(r/b)^2)/2} \begin{Bmatrix} (y - y_0)/b \\ -(x - x_0)/b \\ 0 \end{Bmatrix} \tag{3.1}$$

$$\rho = \rho_\infty \left(1 - \frac{\gamma - 1}{2} \left(\frac{u_A}{c_\infty} \right)^2 e^{1-(r/b)^2} \right)^{1/(\gamma-1)} \tag{3.2}$$

$$p = p_\infty \left(1 - \frac{\gamma - 1}{2} \left(\frac{u_A}{c_\infty} \right)^2 e^{1-(r/b)^2} \right)^{\gamma/(\gamma-1)} \tag{3.3}$$

where $b \simeq 0.08$ which regulates the size of the vortex, $u_A = 0.8V_\infty$, x_0 and y_0 represent the central points of the vortex, and r represents a local radius that originates from these central points and composes the circular shape of the vortex.

Initial shape of the pressure contours of the vortex on non-uniform mesh with 50×50 grid points are shown in Figure 3.1.

After the simulation, pressure contours of the convected vortex for 3 different meshes defined above is shown in Figure 3.2.

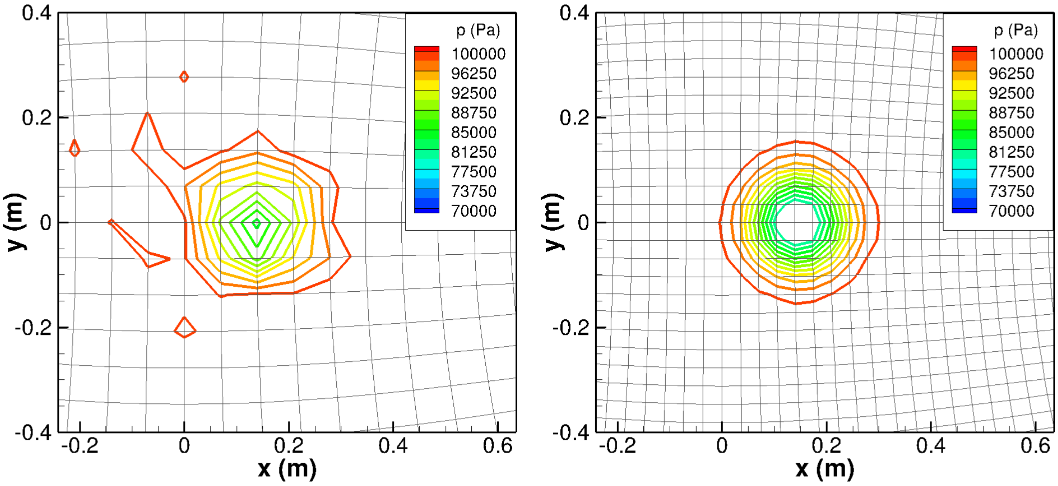

(a) 50 × 50 grid points (b) 100 × 100 grid points

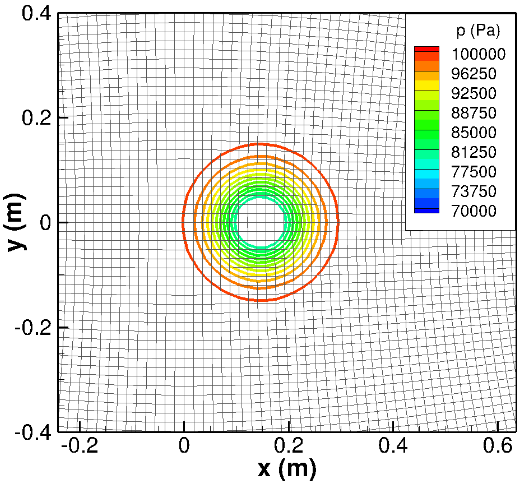

(c) 200 × 200 grid points

Figure 3.2: Pressure contours of the isentropic vortex convected through different mesh domains

Root-mean-square (RMS) of error values caused by the difference between the flow variables of the simulation and the analytical one shows the order of accuracy as follows: 4^{th} order accuracy in 2D space is represented as $\mathcal{O}[(\Delta x)^4,(\Delta y)^4]$. After halving the grid spacings in both direction, the new error should become as $\mathcal{O}[(\Delta x/2)^4,(\Delta y/2)^4] = \mathcal{O}[(\Delta x)^4/16,(\Delta y)^4/16]$.

After the simulation, the RMS of errors caused by the difference of entropy flow values of the isentropic vortex is analyzed. Figure 3.3 shows that the comparison of the RMS curve obtained from the simulations with 2^{nd} and 4^{th} order accuracy curves in logarithmic scales.

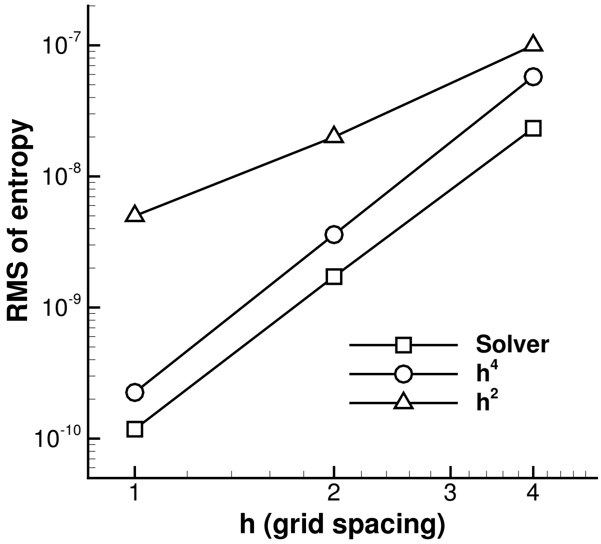

Figure 3.3: RMS values of the entropy flow variables changing with grid spacings

As seen in Figure 3.3, the RMS curve of the simulation is almost parallel with the 4^{th} order accuracy curve. This means that 4^{th} order accuracy is achieved as expected during the development of the solver.

3.2 Testing of Far Field Boundary Reflection

Since outgoing of acoustic waves from the computational boundaries should be non-reflective in aeroacoustic problems, it is useful to check the behaviour of the employed outer boundary conditions. For this purpose, the far field equations (2.18 and 2.19) implemented into the solver are tested with a propagation problem of a 2D pulse. In this problem, outgoing of the propagated pulse from a computational domain without a significant reflection is expected.

The pressure pulse is created by Gaussian distribution at the center of the computational domain ($x = 0.5m, y = 0.5m$) with zero velocity. Freestream pressure value is taken as 101300 Pa. The simulation is done again with Euler equations without artificial dissipation. Solutions are obtained in time accurate manner and propagation of the pulse is observed.

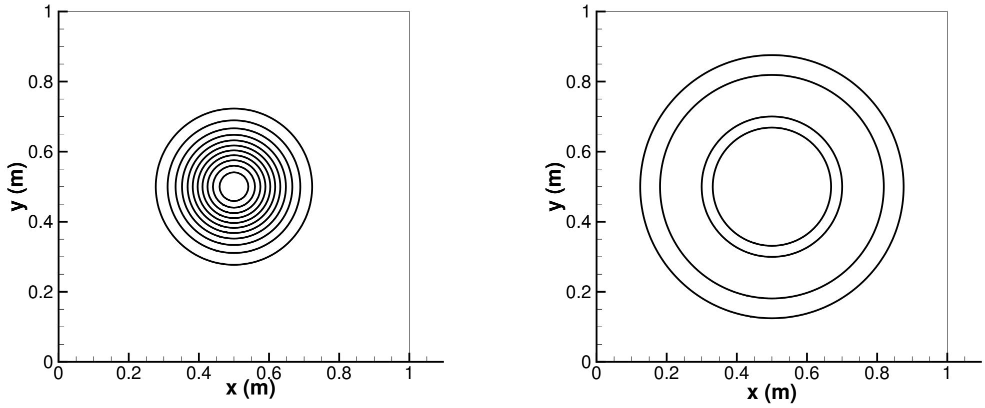

(a) t = 0 s (b) t = 6×10^{-4} s

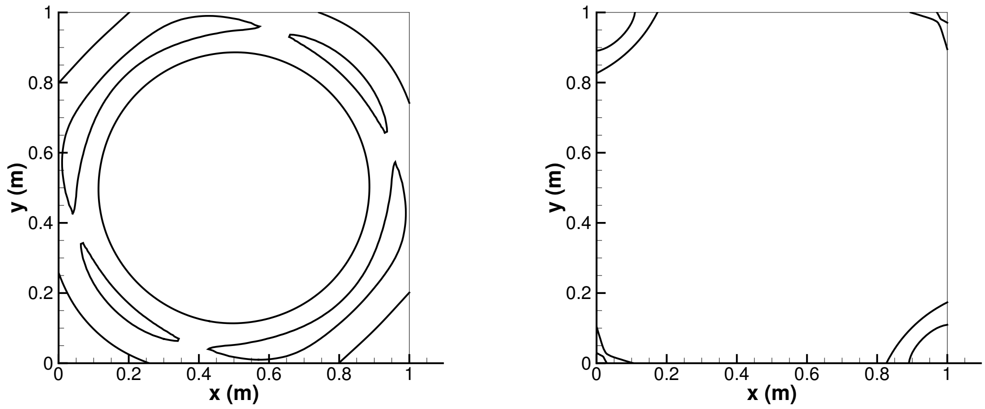

(c) t = 12×10^{-4} s (d) t = 18×10^{-4} s

Figure 3.4: Appearances of the pressure pulse in the computational domain at different times

Figure 3.4 shows several phases during the propagation. The contour plot at $t = 0$ s represents the initial condition of the pulse. Besides, Figure 3.5 demonstrates the cross sections of the pulse taken from the central line ($y = 0.5m$) of the contour plots shown in Figure 3.4.

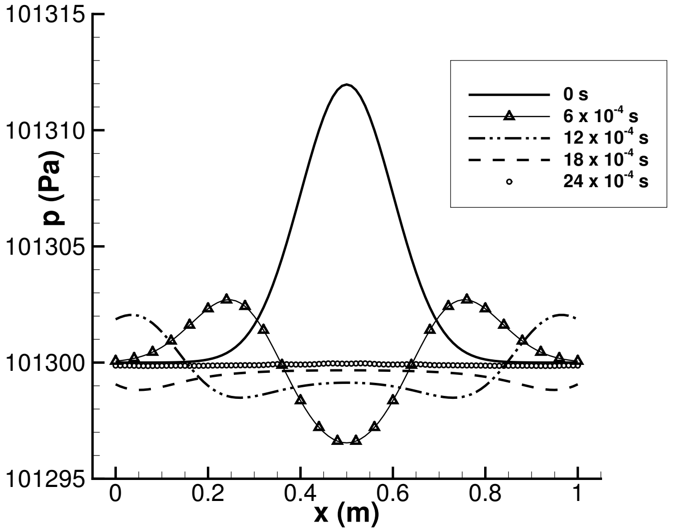

Figure 3.5: Cross section view of the pressure pulse at $y = 0.5m$ at different times

It is observed that the pulse leaves the computational domain without a significant reflection and finally the domain reaches to the ambient pressure value which is 101300 Pa (see Figure 3.5). Consequently, the far field equations (2.18 and 2.19) are used in the further problems in this thesis.

3.3 Testing of Flux Computations

Steady-state problems are more challenging cases to verify the implementations of the flux terms, boundary conditions, and artificial dissipation to the numerical solver. However, high-order methods are not appropriate to the steady-state problems due to a requirement of long iteration periods to reach steady flow conditions inherently. Thus, steady test cases are performed with that knowledge.

Furthermore, many spurious short waves that could not be solved exactly by the introduced scheme come in sight and contaminate the computational domain when, most particularly, the freestream flow is encountered a solid body in numerical simulations. Therefore, artificial dissipation (sufficient to damp only spurious waves) is added for the following problems.

3.3.1 Inviscid Flow over a Cylinder

In this problem, a 2D, steady, inviscid flow simulation over a cylinder body is performed. In this simulation, again Euler equations are solved but this time for a more difficult problem. Steady-state flow solutions around the cylinder are expected.

In the simulation, an inviscid flow with 0.3 Mach is passed over a cylinder. An O type mesh with 129×81 grid points are used. The weight of artificial dissipation term, $\epsilon^{(6)}$, is selected as $1/64$. The flow velocity corresponds to an almost incompressible flow condition. Therefore, symmetric contours are expected around the cylinder.

Residual values of flow variables can be seen in Figure 3.6. It is observed that the simulation is reached to the steady-state condition. A requirement of a long iteration period is due to the use of a high-order method.

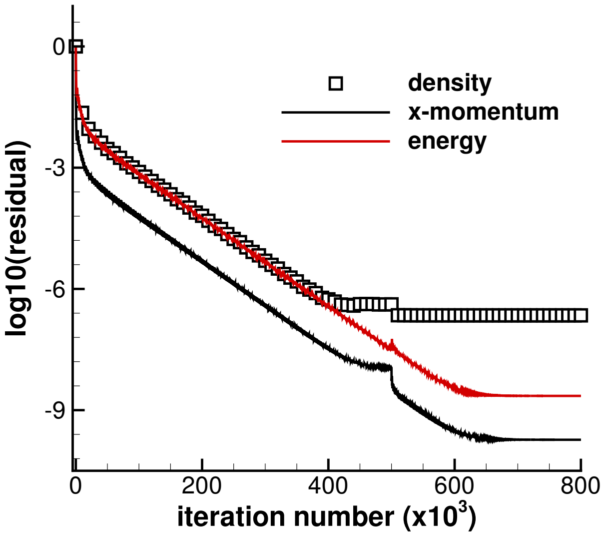

Figure 3.6: Residual values of density, x-momentum and energy flow variables for the inviscid flow over the cylinder test case

Figure 3.7 shows the pressure and Mach contours around the cylinder at the steady-state condition. As seen that symmetry is almost preserved. A comparison of the pressure coefficient, C_p, distribution on the wall surface between the solution of the simulation and the analytical solution (potential flow solution) is done as well. Figure 3.8 demonstrates this comparison.

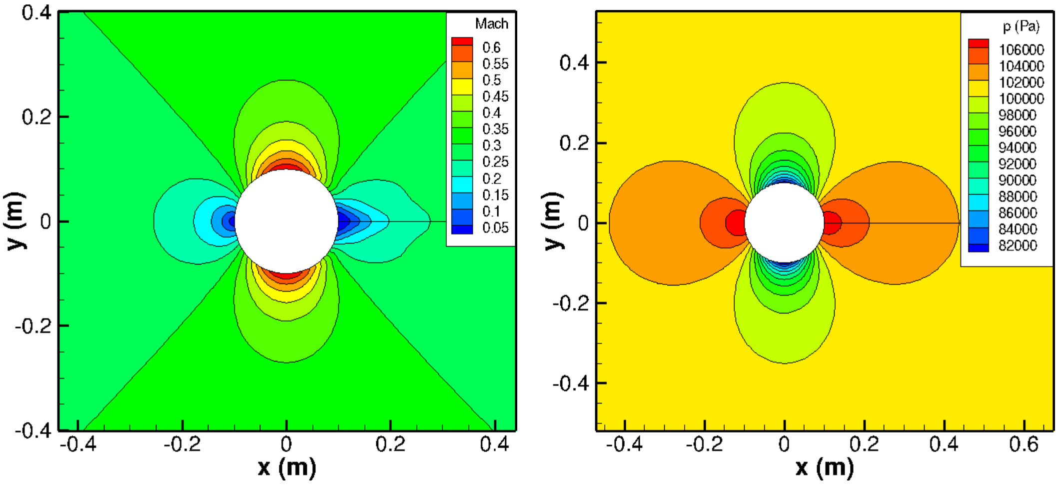

(a) Mach contours

(b) pressure contours

Figure 3.7: Inviscid flow with 0.3 Mach number over a cylinder

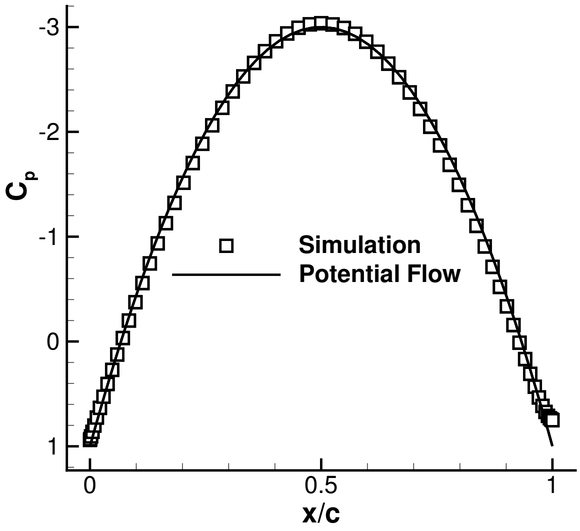

Figure 3.8: Comparison of C_p distribution on the wall with the potential flow solution

Results indicate that a deviation is observed around the trailing edge of the cylinder. This is possibly due to that the artificial dissipation term added to damp out the spurious waves causes such an addition of viscosity. Therefore, there occurs a somewhat boundary layer effect around the trailing edge.

3.3.2 Viscous Flow Test Cases

The aim of this section is to verify the routines in the code that include viscous flux terms of NS equations as well as turbulent viscosity computations through SA equation. First, 2D steady-state laminar and turbulent flow problems over a flat plate are simulated. Then, 2D steady-state laminar flow over a NACA0012 blade section is solved.

3.3.2.1 Laminar Flow over a Flat Plate

A laminar flow with a Reynolds number of 10^5 (chord-based) and 0.2 Mach number over a 2 m-long flat plate is simulated in this section. A mesh domain of the flatplate is shown in Figure 3.9 with the boundary conditions. Since the far field boundary is not far enough away from the wall, Riemann far field conditions are applied instead of the radiation and outflow equations (2.18 and 2.19).

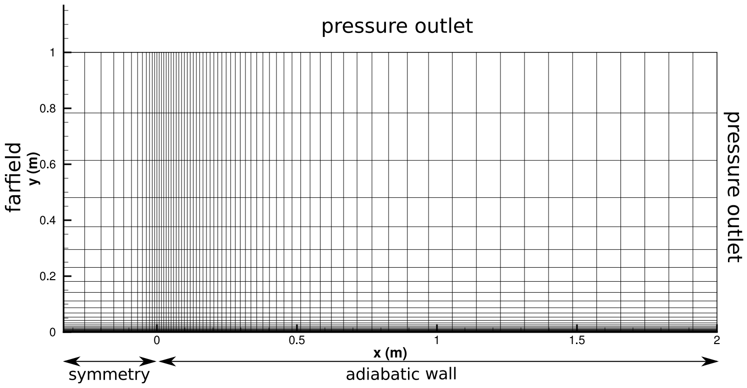

Figure 3.9: Simulation setup with 69×49 grid points for the flat plate test cases

The simulation is performed with NS equations until the steady condition is reached. $\epsilon^{(6)}$ is selected as $1/64$. Residual history of flow variables are demonstrated in Figure 3.10.

After the simulation, velocity profiles of the laminar boundary layer is compared with Blasius solution which is the analytical solution for zero pressure gradient flow. While Figure 3.11 shows this comparison at the middle point of the wall, Figure 3.12 shows it at the trailing edge.

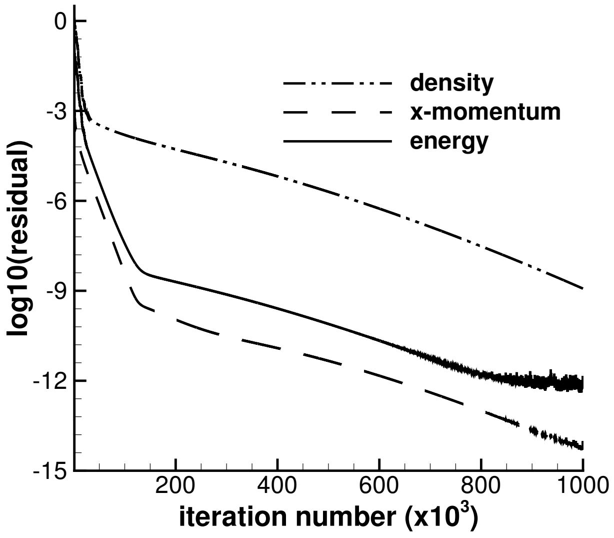

Figure 3.10: Residual values of density, x-momentum and energy flow variables for the laminar flow over the flat plate test case

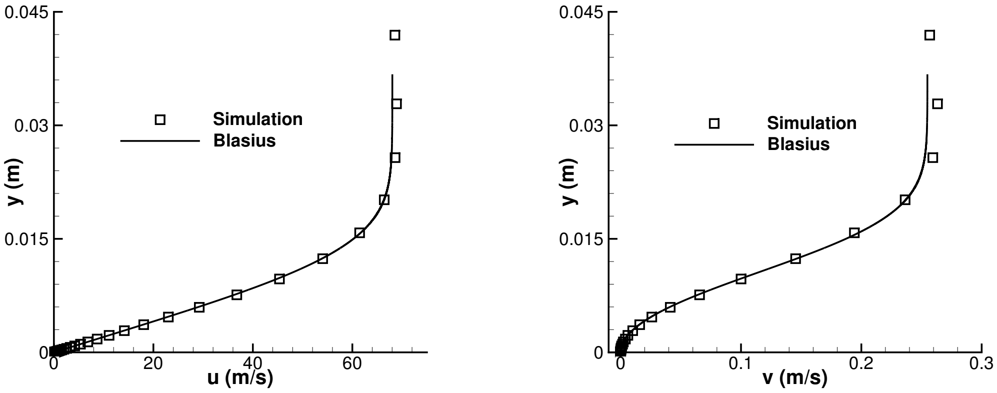

(a) Parallel velocity component to the wall (b) Orthogonal velocity component to the wall

Figure 3.11: Velocity profile in a laminar boundary layer compared with Blasius solution at middle point of the flat plate

As seen in Figures 3.11 and 3.12, laminar velocity profile is obtained nearly the same as Blasius solution. However, since orthogonal velocity component has different order of magnitude, the difference between Blasius one seems much more than in parallel velocity component. It should be indicated that there exist a little more deviation in orthogonal velocity component of the trailing edge results since the boundary layer is getting thicker there.

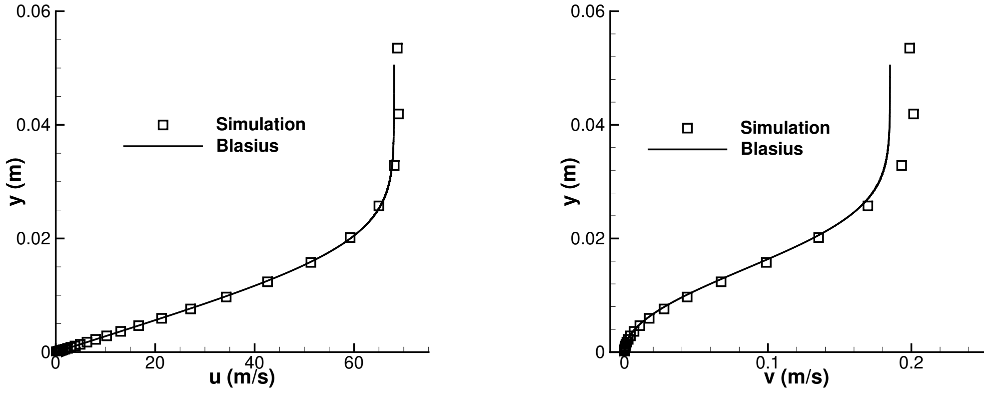

(a) Parallel velocity component to the wall (b) Orthogonal velocity component to the wall

Figure 3.12: Velocity profile in a laminar boundary layer compared with Blasius solution at trailing edge of the flat plate

Skin friction coefficient is also compared with Blasius solution in Figure 3.13. The results match up with each other perfectly.

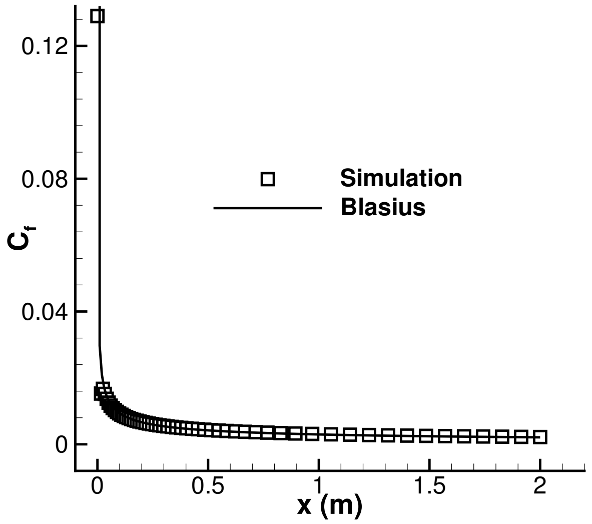

Figure 3.13: Comparison of skin friction coefficient, C_f, with Blasius solution for the laminar flow over the flat plate test case

3.3.2.2 Turbulent Flow over a Flat Plate

In this case, a turbulent flow with a Reynolds number of 10^7 and 0.2 Mach number is passed over the same flat plate. $\epsilon^{(6)}$ is selected as $1/64$. Residual histories can be seen in Figure 3.14. As observed that a level of the convergence to the steady-state condition is not reached to the level of the laminar flow test case. The possible reason is that the stability characteristic of SA equation is different than that of NS equations. Thus, the difference might affect the stability characteristic of fully-turbulent problems. However, this problem is tested to verify the computation routines of the turbulent terms, not to reduce the residual values as in the previous problem.

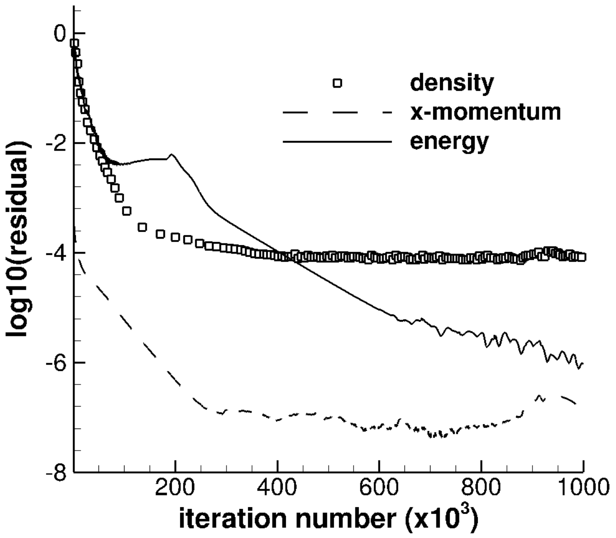

Figure 3.14: Residual values of density, x-momentum and energy flow variables for the turbulent flow over the flat plate test case

Velocity profile is validated with the law of the wall as shown in Figure 3.15. Skin friction coefficient distribution over the plate is also compared with CFL3D code of NASA Langley Research Center [9] which uses 2^{nd} order schemes (see Figure 3.16).

Figure 3.16 shows that although the grids are much more dense in both directions in the mesh of CFL3D solver case (545×385 grid points), friction coefficient distribution is exactly the same (except initial points of the leading edge) as the coarser one. This shows the superiority of the use of 4^{th} order DRP numerical schemes as well.

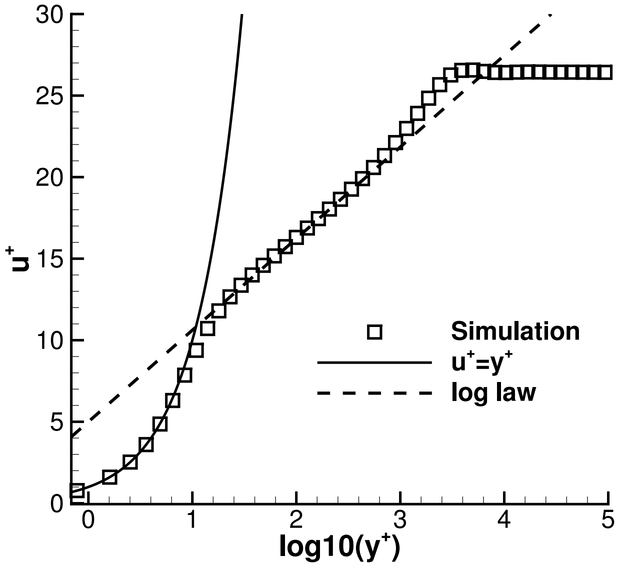

Figure 3.15: Velocity profile in a turbulent boundary layer compared with the law of the wall for the flat plate test case

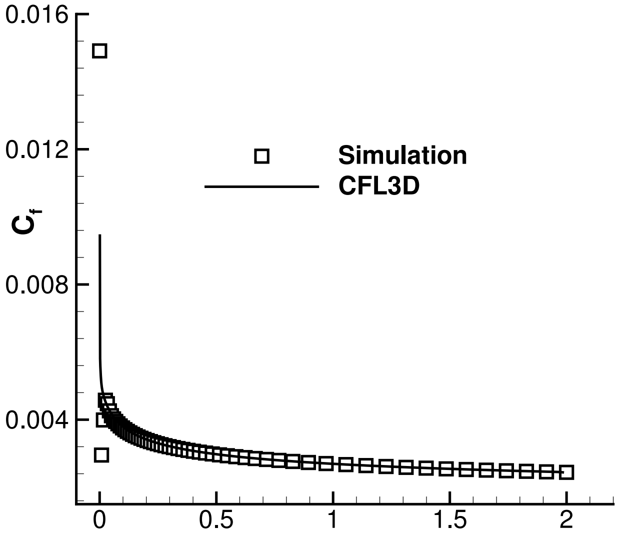

Figure 3.16: Comparison of skin friction coefficient, C_f, with CFL3D code results with 545×385 grid points [9] for the turbulent flow over the flat plate test case

3.3.2.3 Laminar Flow over a NAC0012 Airfoil

A laminar flow over a NACA0012 airfoil is simulated with the conditions of 0.5 Mach, zero angle of attack, and a Reynolds number of 5000. The simulation is performed with NS equations. O type mesh with 157×113 grid points shown in Figure 3.17 is used. Again $\epsilon^{(6)}$ is selected as $1/64$.

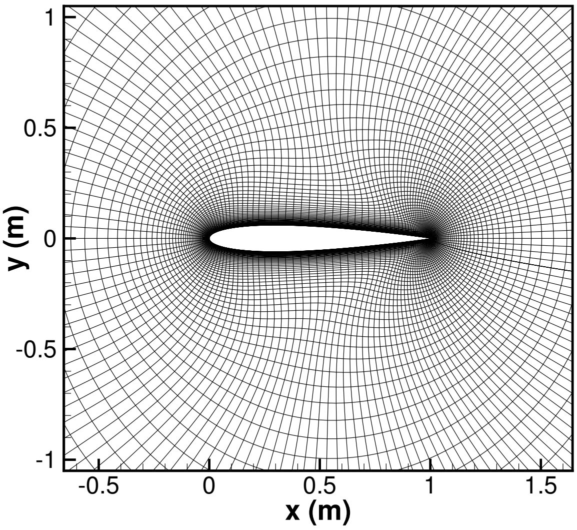

Figure 3.17: O type mesh domain with 157×113 grid elements over a NACA0012 airfoil for the laminar flow test case

Results are compared with the study of Villedieu et al. [69] where the same problem was simulated by high order upwind schemes with an unstructured C type mesh with 8564 grid elements (200 of them are on the airfoil surface).

Residual values of flow variables are demonstrated in Figure3.18.

While Figure 3.19 shows the attained Mach and pressure contours, Figure 3.20 shows the C_p and C_f distributions over the airfoil.

It is evident from the figures, the distributions are quite similar with the study of Villedieu et al. except the leading and trailing edges (see Figure 3.20(b)). The reason of the deviation at the leading and trailing edges is due to relatively poor mesh density in the present calculations. Besides, because of the O type mesh configuration, wake leaving from the trailing edge is not resolved as well as on a C type mesh.

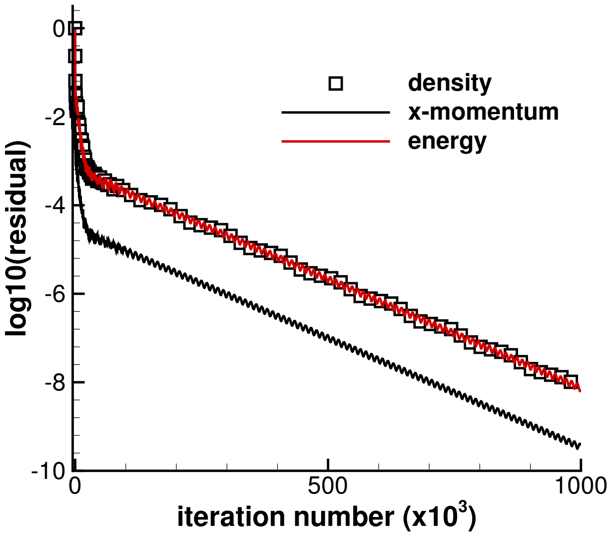

Figure 3.18: Residual values of density, x-momentum and energy flow variables for the laminar flow over a NACA0012 airfoil test case

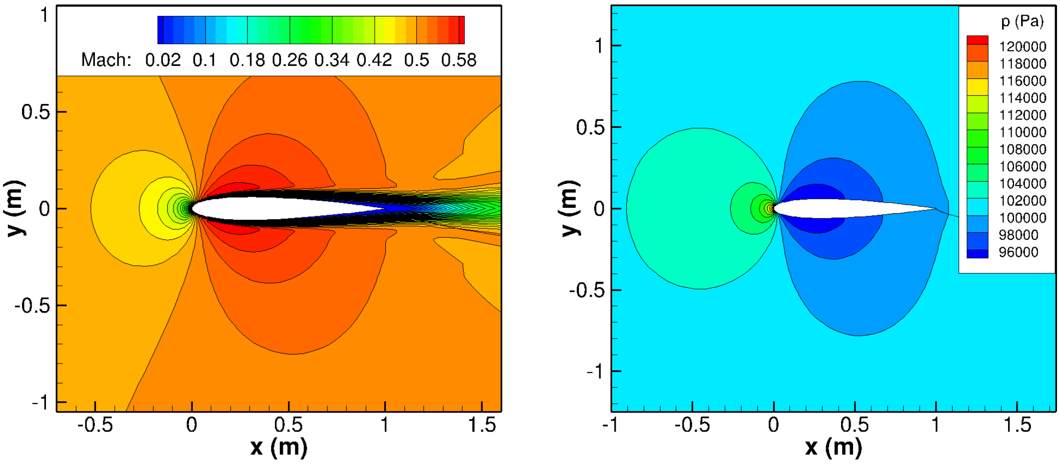

(a) Mach contours

(b) pressure contours

Figure 3.19: Contours of laminar flow around a NACA0012 blade section

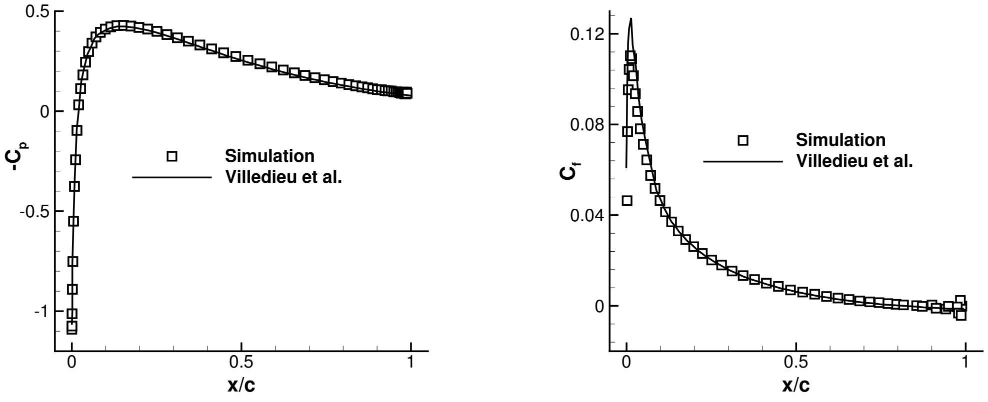

(a) pressure coefficient

(b) skin friction coefficient

Figure 3.20: C_p and C_f comparisons with the study of Villedieu et al. [69]

3.4 Testing of Implementation of Turbulence Modelling

The fact that DDES approach can delay the activation of LES in boundary layers in case of 'severe' grids describes the superiority of DDES to DES. This is why DDES approach is preferred in this study. To validate the implementation of DDES algorithm to the solver, a severe grid is created along the flat plate mesh domain which is shown in Figure 3.9. Severe grids occur when a grid spacing parallel to the wall is less than the boundary layer thickness. Therefore, the mesh domain is extended through z direction and grid spacings in x and z directions are rearranged to be able to have a severe grid. Boundary conditions and the mesh topology in y direction of the mesh are not changed.

General view of the severe grid is shown in Figure 3.21. Δx and Δz are selected as 0.1δ where δ is the boundary layer thickness, and calculated as $\delta = 0.37(Re_L)^{-0.2}L$ [54]. The mesh has $513 \times 49 \times 9$ grid points.

An unsteady turbulent flow with a Reynolds number of 10^6 in x direction and 5×10^4 in z direction, and 0.1 Mach number over 2 m-long flat plate is simulated with RANS, DES, and DDES, separately. It is expected that while DES could not capture the eddy viscosity distribution in the boundary layer, DDES gives a closer result to RANS in the severe grid. The simulation is carried on until time-averaged flow variables do not

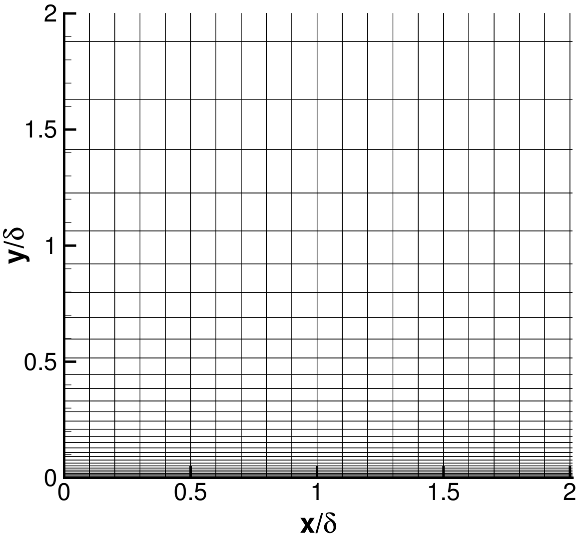

Figure 3.21: View of severe grid with $\Delta x \simeq \Delta z \simeq 0.1\delta$

change. $\epsilon^{(6)}$ is selected as $1/64$. Distributions of turbulent eddy viscosity to molecular kinematic viscosity, ν_t/ν, and f_d function, which is used in DDES algorithm to postpone LES mode, in the boundary layer are shown in Figure 3.22.

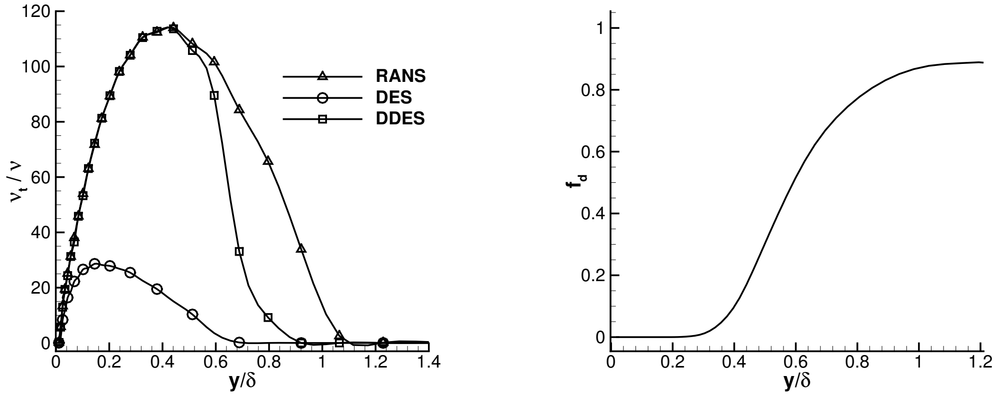

(a) $\tilde{\nu}/\nu$

(b) f_d function

Figure 3.22: Distributions of ν_t/ν and f_d function in the flat plate boundary layer

Figures 3.22(a) and 3.22(b) indicate that DDES delays the activation of LES mode by f_d function and develops much more closer eddy viscosity distribution to RANS than DES as expected. While DDES preserves the peak eddy viscosity, DES reduces it by almost 75% and this was also concluded by Spalart et al. in their study introducing DDES algorithm [58].

3.5 Unsteady Aeroacoustic Simulation of a Blade Section

In this section, it is aimed to detect the turbulent structures emitted noise from a wind turbine blade section to an observer. In order to make comparisons, a PhD study of Wei Jun Zhu, titled as "Aero-Acoustic Computations of Wind Turbines" [75], is selected as a benchmark case.

The properties of the simulation to be compared with the benchmark case are summarized as follows:

- A 2D uniform flow with a Reynolds number of 10^5, 0.2 Mach number, and 5^0 angle of attack is passed over a wind turbine blade section.
- The blade section has a NACA0012 airfoil profile.
- O type mesh with 225 grid points in the circumferential direction, and 153 grid points in the radial direction is constituted (see Figure 3.23).
- The first grid spacing starting from the airfoil surface towards the radial direction is 1.2×10^{-4} length of the chord.
- Oncoming flow has a continuous (ambient) eddy viscosity as $\tilde{\nu} = 3\nu_\infty$ which is suggested by Spalart [59] to obtain fully-turbulent flow.
- An observer is located at 2.5 chord length away from the trailing edge towards the radial direction which corresponds to a point of $(x, y) = (1.0, 2.5)$ in the computational domain.

It is not possible to make direct numerical resolution up to the observer location because of high cost of mesh requirement. Therefore, after unsteady, and vortical flow solutions near the blade are reached to a condition which is sufficient to collect noise data, the perturbation flow values at the observer location are calculated by FW-H

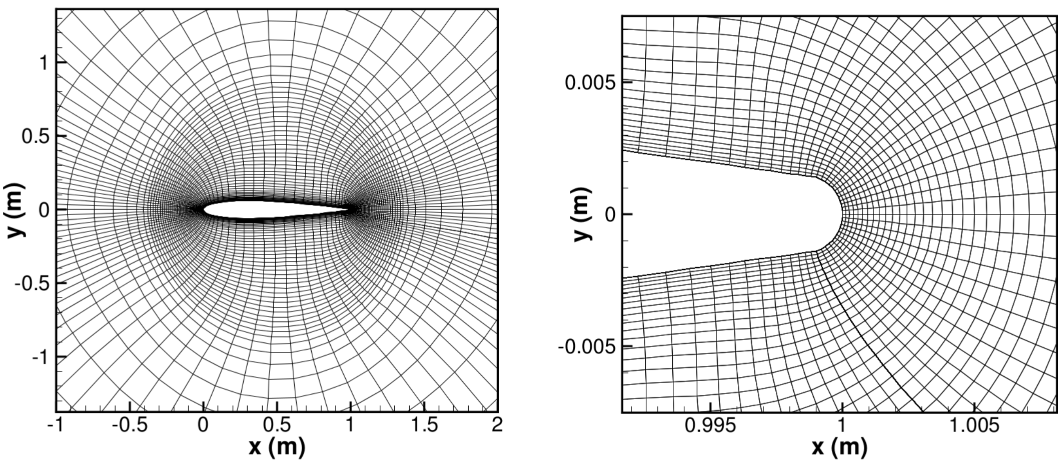

(a) near field (illustrated with odd-numbered nodes)

(b) trailing edge field

Figure 3.23: View of the mesh around the airfoil with 225×153 grid ponits

integral equation. Then, sound pressure levels (SPL) of the observer location in a frequency domain are calculated as:

$$SPL(dB) = 20log10\left(\frac{p'/\sqrt{2}}{p_{ref}}\right) \tag{3.4}$$

where $p_{ref} = 2 \times 10^{-5}$ Pa.

3.5.1 Grid Dependency Study

Before starting the simulation, a grid dependency study is performed. This study basically shows whether the mesh is both fine enough to obtain desired solutions and coarse enough to reduce the computation cost or not. Comparing the time-averaged flow variables obtained from different mesh domains is the most appropriate way to make grid dependency study. However, it is computationally expensive for high Reynolds number flow problems. Instead, developed 2D flow solutions just before beginning of the unsteadiness are decided to be compared. For this purpose, 3 different mesh domains are created. One of them is the original mesh introduced in Figure 3.23. Others are the coarsened mesh where the grid points are halved and the refined mesh where the grid points are doubled in both directions. The coarsened mesh is created by removing even-numbered nodes of the original mesh. On the other hand, the refined mesh is created by an addition of extra nodes between each node of the original mesh bi-quadratically. The skin friction coefficients obtained from each mesh at the same convection time are compared and demonstrated in Figure 3.24.

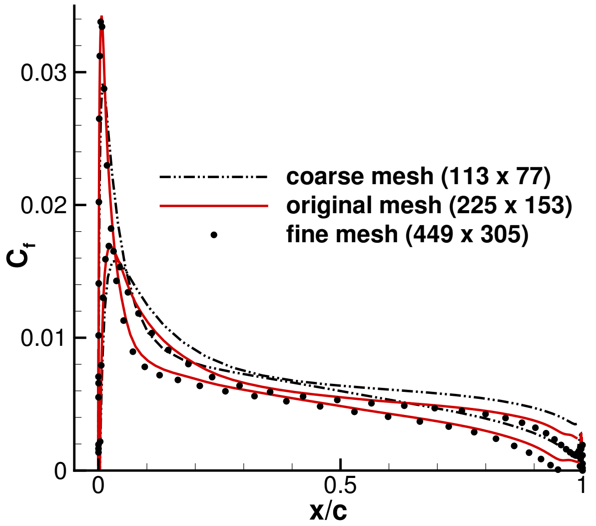

Figure 3.24: Grid dependency study for 3 different mesh domains

The results indicate that the solutions of the original and refined mesh domains are close each other. However, that of the coarsened one deviates from others noticeably. Therefore, the use of original one is plausible considering the computational cost.

3.5.2 Unsteady Flow Results

The simulation is performed with DDES approach and carried on until dimensionless time about 150 (with respect to speed of sound). During the simulation 64 processors are used. Time step is around 5×10^{-5} dimensionless time (with respect to speed of sound) which corresponds to CFL number of 0.8. $\epsilon^{(6)}$ is selected as $1/64$. Fully-turbulent results are shown in Figure 3.25.

The results in Figure 3.25 indicate that a separation and vortical flow structures start to occur between $x/c = 0.2$ and $x/c = 0.3$ along the surface. In the benchmark case which was performed with 2^{nd} order methods and LES approach, the separation occurred almost at the same region.

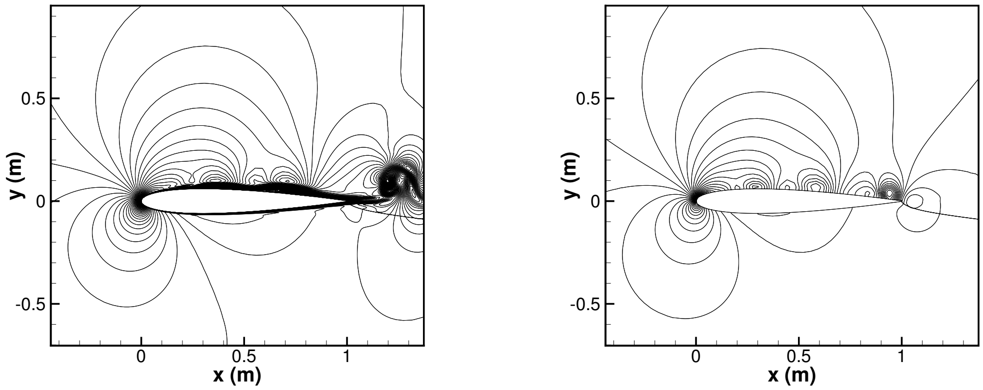

(a) Mach field (b) pressure field

Figure 3.25: Fully-turbulent flow fields over a NACA0012 blade section with Re=10^5, α=5^0, Mach=0.2

Flow data, required for FW-H integral equation, is collected on a permeable FW-H surface which surrounds almost all turbulent flow structures around the blade section. The permeable surface is selected as the boundary surface which distinguishes much coarser and much finer grid domains (see Figure 3.26). The fact that how often and how long should flow data be collected is decided with respect to a resolution capacity of the solver and the mesh. The boundaries of the resolution capacity are analyzed according to maximum and minimum wave frequencies. Hence, maximum and minimum frequencies in the domain surrounded by the permeable surface are found as follows:

One wave can be resolved with approximately 6 grid spacings by this solver. Maximum wave frequency that can be resolved is computed as:

$$f_{max,resolved} = \frac{c}{6\Delta x_{min}} \simeq 4250Hz \tag{3.5}$$

where c is the speed of sound. Then, minimum period to collect data is:

$$T_{min} = \frac{1}{f_{max,resolved}} \simeq 2.4 \times 10^{-4}s \tag{3.6}$$

which corresponds to 200 iteration numbers in the solver. This means data should be collected in each 200 iterations. On the other hand, maximum period is selected as one convection time which corresponds to approximately 120000 iteration numbers. Minimum frequency is, then, found as 50 Hz.

After data collection is finished, all data are transformed to the frequency domain by Fast Fourier Transform. Pressure fluctuation amplitudes ($|\hat{p}|$) and turbulent kinetic energy (TKE) for different frequency values at different locations on the permeable surface are presented in Figure 3.27. Figure 3.26 shows FW-H surface and these locations.

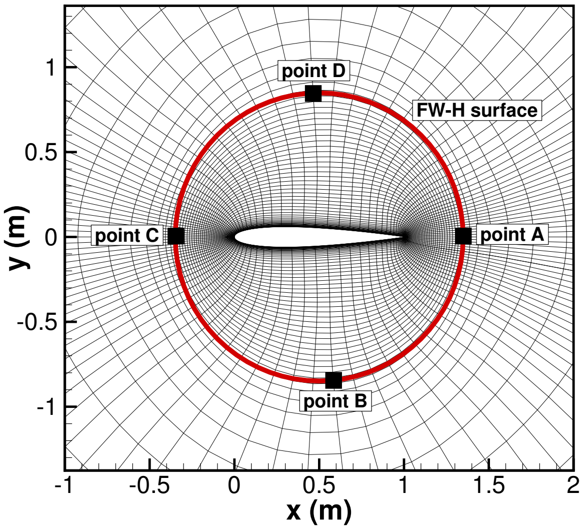

Figure 3.26: FW-H surface and the points where fluctuations are obtained

Figure 3.27 indicates that intenseness of turbulent structures is increasing through trailing edge. While point C has lowest intensity of TKE, point A has approximately 2000 times of that of point C. On the other hand, pressure fluctuation which is directly related to acoustic spectra is reached its minimum value at point C as well. It is hard to compare the other points from the pressure fluctuations. When the pressure levels of each point are obtained by p'_{rms}/p_{ref}, it is seen in Figure 3.28 that points B, and D have similar trends in pressure levels distributions so that they cause similar noise levels. The reason is that sound is radiated in all direction and they are both located in regions close to unsteady, and vortical turbulent flow structures. Moreover, point A has still been encountered vorticity fields. Therefore, making a noise comment about it could be misleading.

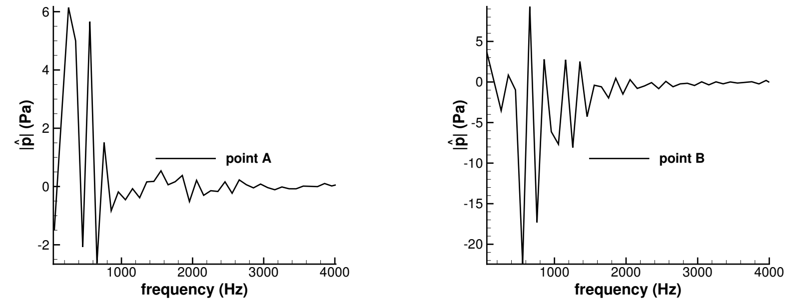

(a) $|\hat{p}|$ at point A (b) $|\hat{p}|$ at point B

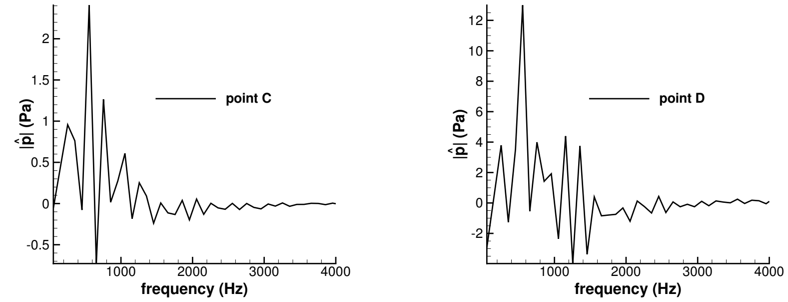

(c) $|\hat{p}|$ at point C (d) $|\hat{p}|$ at point D

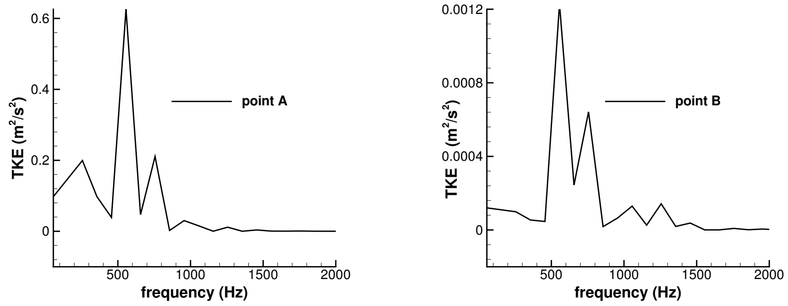

(e) TKE at point A (f) TKE at point B

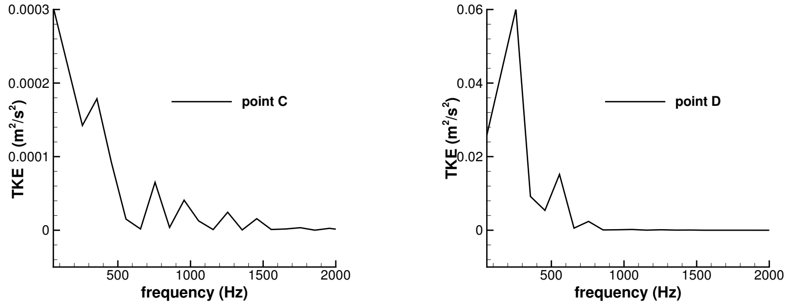

(g) TKE at point C (h) TKE at point D

Figure 3.27: Distributions of pressure fluctuation amplitudes and turbulent kinetic energy at different points on FW-H surface

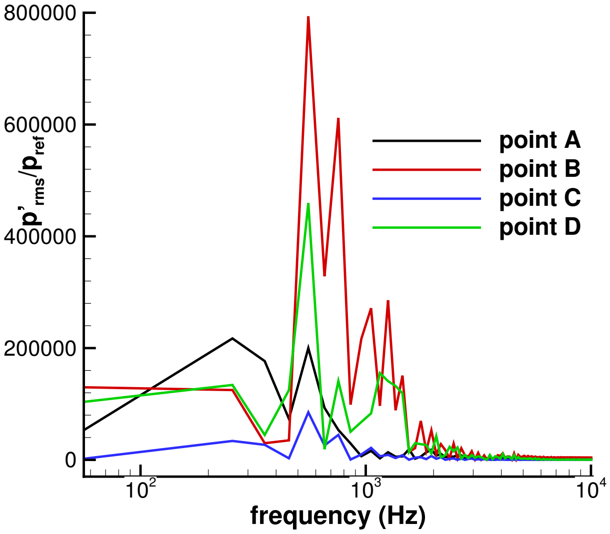

Figure 3.28: Pressure levels of different points located on FW-H surface with respect to frequency values in logarithmic scale

The sound pressure level of the observer located far from the blade section is not computed since FW-H integral equation has not been validated yet. In the following studies, after it is validated, the SPL distribution will be compared with the results of the benchmark case.

CHAPTER 4

CONCLUSION

In this thesis, a 4^{th} order, dispersion-relation-preserving, parallel, finite difference solver of Navier-Stokes equations and Spalart-Allmaras one equation model with DDES capability is developed for the purpose of performing aeroacoustic simulations around wind turbine blade sections.

Firstly, the reason why a non-dispersive and non-dissipative solver is required in Computational Aeroacoustic simulations is explained. Then, numerical methodologies including the way of spatial and temporal discretizations that provide 4^{th} order, DRP features within the computational domains with appropriate boundary conditions and artificial dissipation are described in the frame of acoustic uses.

At the beginning of the results section, validation test problems are carried on. By the vortex convection problem, the achievement of the 4^{th} order accuracy is shown. In the propagation problem of the pressure pulse, outgoing of the pulse from a computational domain without a significant reflection is provided as desired with the far field equations based on asymptotic solutions of the linearized Euler equations. The computation routines of inviscid, viscous, and turbulent flux terms of the solver are verified with the steady-state problems involving flow over a solid body situations. Furthermore, the effect of the artificial dissipation on flow solutions is observed in the steady-state problems. Although in the inviscid flow over a cylinder problem artificial dissipation has caused a boundary-layer effect around the trailing edge due to the addition of viscosity, the pressure coefficient distribution is almost matched with the potential flow solution. In the laminar flow over a flatplate problem, the artificial dissipation has worked perfect such that residual histories could be reduced to

-15 levels in logarithmic scales. However, in the turbulent case it is observed that the artificial dissipation method for SA one equation model should be constructed differently than NS equations. Nevertheless, the solutions of the velocity profile and the skin friction distribution have shown highly satisfactory results even with coarse mesh domains with the help of 4^{th} order and DRP scheme.

Finally, the unsteady simulation of a fully-turbulent flow over a NACA0012 wind turbine blade section is conducted via DDES approach. The flow solutions are compared with the results of the benchmark test case which was done by 2^{nd} order methods and LES approach in literature. After the simulation, the vortical flow structures that cause noise are observed along the surface. A similar separation trend is observed when compared with the benchmark case. Moreover, pressure fluctuations and turbulent kinetic energy of different points located on FW-H surface which is a permeable surface are compared with each other. It is observed that the region near the leading edge develops fewest noise levels since turbulent structures do not occur around the leading edge. Point A has the biggest turbulent kinetic energy distribution since it is exposed to vorticity fields directly. Points B and D have similar pressure levels, which are related to acoustic spectra, since sound is radiated in all direction and these points have similar distances to the turbulent structures around the blade section.

It should be emphasised that this thesis mostly includes the development process of the solver. Therefore, the validation problems constitutes the major part of the thesis. However, this solver is created for unsteady simulations and noise predictions around wind turbine blade sections. Hence, as an immediate future work, implementation of FW-H integral equation will be validated so that noise levels of far away regions could be obtained and compared with experimental and numerical studies in literature. Furthermore, comprehensive studies including 3D and blade tip effects, thicker blade sections, synthetic inlet conditions, transition behaviour, and large separations can be analysed in details by this solver. Then, acoustic spectra of these studies can be revealed. Moreover, acoustic simulations for whole wind turbine blades can be performed and blade shape optimization studies to reduce the noise levels can be conducted.

REFERENCES

[1] Z. Abdmouleh, R. A. Alammari, and A. Gastli. Review of policies encouraging renewable energy integration & best practices. *Renewable and Sustainable Energy Reviews*, 45:249–262, 2015.

[2] ANSYS. Fluent flow solver software. `http://www.ansys.com`.

[3] A. Bayliss and E. Turkel. Far field boundary conditions for compressible flows. *Journal of Computational Physics*, 48(2):182–199, 1982.

[4] F. Bertagnolio. *Trailing edge noise model applied to wind turbine airfoils*. Forskningscenter Risø Roskilde, 2008.

[5] C. Bogey and C. Bailly. Three-dimensional non-reflective boundary conditions for acoustic simulations: far field formulation and validation test cases. *Acta Acustica united with Acustica*, 88(4):463–471, 2002.

[6] G. Boyle. *Renewable energy*. OXFORD university press, 2004.

[7] CD-adapco. Star-cd flow solver software. `http://www.cd-adapco.com`.

[8] K. Cengiz and Y. Özyörük. Rüzgar türbini aeroakustiği benzetimi maksadıyla yüksek doğruluklu üç boyutlu navier-stokes kodu geliştirilmesi. In *Ulusal Havacılık ve Uzay Kongresi*, pages UHUK–2014–101, 2014.

[9] N. L. R. Center. Turbulence modeling resource. `http://turbmodels.larc.nasa.gov/flatplate_sa.html`. [accessed August-2014].

[10] T. Colonius and S. K. Lele. Computational aeroacoustics: progress on nonlinear problems of sound generation. *Progress in Aerospace sciences*, 40(6):345–416, 2004.

[11] D. Crighton. Basic principles of aerodynamic noise generation. *Progress in Aerospace Sciences*, 16(1):31–96, 1975.

[12] A. Crivellini and V. D'Alessandro. Spalart–Allmaras model apparent transition and RANS simulations of laminar separation bubbles on airfoils. *International Journal of Heat and Fluid Flow*, 47:70–83, June 2014.

[13] L. Davidson. Fluid mechanics, turbulent flow and turbulence modeling. *Chalmers University of Technology, Goteborg, Sweden (Nov 2011)*, 2011.

[14] S. Deck. Recent improvements in the Zonal Detached Eddy Simulation (ZDES) formulation. *Theoretical and Computational Fluid Dynamics*, 26:523–550, 2012.

[15] C. Doolan, D. J. Moreau, and L. A. Brooks. Wind turbine noise mechanisms and some concepts for its control. *Acoustics Australia*, 40(1):7–13, 2012.

[16] U. EIA. Annual energy outlook 2013. *US Energy Information Administration, Washington, DC*, 2013.

[17] F. Farassat. Linear acoustic formulas for calculation of rotating blade noise. *AIAA journal*, 19(9):1122–1130, 1981.

[18] F. Farassat. Introduction to generalized functions with applications in aerodynamics and aeroacoustics. 1994.

[19] C. S. Ferreira, H. Bijl, G. Van Bussel, and G. Van Kuik. Simulating dynamic stall in a 2d vawt: Modeling strategy, verification and validation with particle image velocimetry data. In *Journal of Physics: Conference Series*, volume 75, page 012023. IOP Publishing, 2007.

[20] O. Fleig, M. Iida, and C. Arakawa. Wind turbine blade tip flow and noise prediction by large-eddy simulation. *Journal of solar energy engineering*, 126(4):1017–1024, 2004.

[21] M. B. Giles. Nonreflecting boundary conditions for euler equation calculations. *AIAA journal*, 28(12):2050–2058, 1990.

[22] M. Gruber, M. Azarpeyvand, and P. Joseph. Airfoil trailing edge noise reduction by the introduction of sawtooth and slitted trailing edge geometries. *integration*, 10:6, 2010.

[23] G. W. E. C. (GWEC). Global statistics. `http://www.gwec.net/global-figures/graphs/`.

[24] T. Hagstrom and I. Nazarov. Absorbing layers and radiation boundary conditions for jet flow simulations. In *Proc. of the 8th AIAA/CEAS aeroacoustics conference*, volume 60, 2002.

[25] R. Hixon and E. Turkel. Compact implicit maccormack-type schemes with high accuracy. *Journal of Computational Physics*, 158(1):51–70, 2000.

[26] F. Hu, M. Hussaini, and J. Manthey. Low-dissipation and low-dispersion runge–kutta schemes for computational acoustics. *Journal of Computational Physics*, 124(1):177–191, 1996.

[27] F. Q. Hu. On absorbing boundary conditions for linearized euler equations by a perfectly matched layer. *Journal of Computational Physics*, 129(1):201–219, 1996.

[28] T. Ikeda, T. Atobe, and S. Takagi. Direct simulations of trailing-edge noise generation from two-dimensional airfoils at low reynolds numbers. *Journal of Sound and Vibration*, 331(3):556–574, 2012.

[29] IRENA. International renewable energy agenda. `http://www.irena.org`.

[30] A. Jameson. Numerical solutions of the euler equations for compressible inviscid flows. *Princeton University, MAE Report*, 1643, 1983.

[31] A. Jameson, W. Schmidt, and E. Turkel. Numerical solutions of the Euler equations by finite volume methods using Runge-Kutta time-stepping schemes. *AIAA paper*, M:1–19, 1981.

[32] M. Kamruzzaman, T. Lutz, W. Würz, W. Z. Shen, W. J. Zhu, M. O. L. Hansen, F. Bertagnolio, and H. A. Madsen. Validations and improvements of airfoil trailing-edge noise prediction models using detailed experimental data. *Wind Energy*, 15(1):45–61, 2012.

[33] T. Kim, M. Jeon, S. Lee, and H. Shin. Numerical simulation of flatback airfoil aerodynamic noise. *Renewable Energy*, 65:192–201, 2014.

[34] G. R. Kirchhoff. Theorie der lichtstrahlen. *Annalen der Physik und Chemie*, 18:663–695, 1883.

[35] L. C. Lau, K. T. Lee, and A. R. Mohamed. Global warming mitigation and renewable energy policy development from the kyoto protocol to the copenhagen accord—a comment. *Renewable and Sustainable Energy Reviews*, 16(7):5280–5284, 2012.

[36] X.-d. Li, M. Jiang, J.-h. Gao, D.-k. Lin, L. Liu, and X.-y. Li. Recent advances of computational aeroacoustics. *Applied Mathematics and Mechanics*, 36(1):131–140, 2015.

[37] M. J. Lighthill. On sound generated aerodynamically. i. general theory. *Proceedings of the Royal Society of London. Series A. Mathematical and Physical Sciences*, 211(1107):564–587, 1952.

[38] D. P. Lockard. An efficient, two-dimensional implementation of the ffowcs williams and hawkings equation. *Journal of Sound and Vibration*, 229(4):897–911, 2000.

[39] D. P. Lockard and J. H. Casper. Permeable surface corrections for ffowcs williams and hawkings integrals. In *Proceedings of the 11th AIAA/CEAS Aeroacoustics Conference, numéro AIAA-2005-2995*, 2005.

[40] R. R. Mankbadi, S. Shih, D. HIXON, J. Stuart, and L. Povinelli. Extension of near field to far field jet noise prediction. In *AIAA Paper-96-2651*. 1996.

[41] A. T. Moorhouse, M. Hayes, S. Von Hünerbein, B. Piper, and M. Adams. Research into aerodynamic modulation of wind turbine noise: final report. 2007.

[42] D. Moroianu and L. Fuchs. Numerical simulation of wind turbine noise generation and propagation. In *Direct and Large-Eddy Simulation VI*, pages 545–554. Springer, 2006.

[43] P. J. Morris, Y. Du, and K. Kara. Reprint of: Jet noise simulations for realistic jet nozzle geometries. *Procedia IUTAM*, 1:28–37, 2010.

[44] S. Oerlemans. *Detection of aeroacoustic sound sources on aircraft and wind turbines*. University of Twente, 2009.

[45] S. Oerlemans and J. Schepers. Prediction of wind turbine noise and validation against experiment. *International journal of aeroacoustics*, 8(6):555–584, 2009.

[46] S. Oerlemans, P. Sijtsma, and B. Mendezlopez. Location and quantification of noise sources on a wind turbine. *Journal of Sound and Vibration*, 299(4-5):869–883, 2007.

[47] Y. Özyörük and L. N. Long. A new efficient algorithm for computational aeroacoustics on parallel processors. *Journal of Computational Physics*, 125(1):135–149, 1996.

[48] R. R. Parchen and T. P. D. TNO-TH. *Progress report DRAW: A prediction scheme for trailing edge noise based on detailed boundary layer characteristics*. TNO Institute of Applied Physics, 1998.

[49] E. Pedersen and K. P. Waye. Perception and annoyance due to wind turbine noise—a dose–response relationship. *The Journal of the Acoustical Society of America*, 116(6):3460–3470, 2004.

[50] T. J. Poinsot and S. Lelef. Boundary conditions for direct simulations of compressible viscous flows. *Journal of computational physics*, 101(1):104–129, 1992.

[51] G. Raman. Wind turbines: clean, renewable and quiet? *Noise Notes*, 9(1):35–44, 2010.

[52] J. Riou, E. Garnier, S. Deck, and C. Basdevant. Improvement of Delayed-Detached Eddy Simulation Applied to Separated Flow over Missile Fin. *AIAA Journal*, 47(2):345–360, 2009.

[53] A. L. Rogers and J. F. Manwell. Wind turbine noise issues. *Renewable Energy Research Laboratory, University of Massachusetts*, 2004.

[54] H. Schlichting, K. Gersten, and K. Gersten. *Boundary-layer theory*. Springer Science & Business Media, 2000.

[55] B. A. Singer, K. S. Brentner, D. P. Lockard, and G. M. Lilley. Simulation of acoustic scattering from a trailing edge. *Journal of Sound and Vibration*, 230(3):541–560, 2000.

[56] P. Spalart and S. Allmaras. A one-equation turbulence model for aerodynamic flows. In *30th Aerospace Sciences Meeting and Exhibit*, Aerospace Sciences Meetings. American Institute of Aeronautics and Astronautics, Jan. 1992.

[57] P. R. Spalart. Detached-eddy simulation. *Annual Review of Fluid Mechanics*, 41:181–202, 2009.

[58] P. R. Spalart, S. Deck, M. Shur, K. Squires, M. K. Strelets, and A. Travin. A new version of detached-eddy simulation, resistant to ambiguous grid densities. *Theoretical and computational fluid dynamics*, 20(3):181–195, 2006.

[59] P. R. Spalart and C. L. Rumsey. Effective inflow conditions for turbulence models in aerodynamic calculations. *AIAA journal*, 45(10):2544–2553, 2007.

[60] A. Tadamasa and M. Zangeneh. Numerical prediction of wind turbine noise. *Renewable Energy*, 36(7):1902–1912, 2011.

[61] C. K. Tam. Computational aeroacoustics: an overview of computational challenges and applications. *International Journal of Computational Fluid Dynamics*, 18(6):547–567, 2004.

[62] C. K. Tam and Z. Dong. Wall boundary conditions for high-order finite-difference schemes in computational aeroacoustics. *Theoretical and Computational Fluid Dynamics*, 6(5-6):303–322, 1994.

[63] C. K. Tam and H. Shen. Direct computation of nonlinear acoustic pulses using high order finite difference schemes. *AIAA paper*, 4325:1993, 1993.

[64] C. K. Tam and J. C. Webb. Dispersion-relation-preserving finite difference schemes for computational acoustics. *Journal of computational physics*, 107(2):262–281, 1993.

[65] C. K. Tam, J. C. Webb, and Z. Dong. A study of the short wave components in computational acoustics. *Journal of Computational Acoustics*, 1(01):1–30, 1993.

[66] C. K. W. Tam. Computational Aeroacoustics : Issues and Methods. *AIAA Journal*, 33(10), 1995.

[67] G. Van den Berg. Effects of the wind profile at night on wind turbine sound. *Journal of sound and vibration*, 277(4):955–970, 2004.

[68] N. Veritas. *Guidelines for design of wind turbines*. Det Norske Veritas: Wind Energy Department, Ris National Laboratory, 2002.

[69] N. Villedieu, T. Quintino, M. Vymazal, and H. Deconinck. High order residual distribution schemes based on multidimensional upwinding. In N. Kroll, H. Bieler, H. Deconinck, V. Couaillier, H. Ven, and K. Sørensen, editors, *ADIGMA - A European Initiative on the Development of Adaptive Higher-Order Variational Methods for Aerospace Applications*, volume 113 of *Notes on Numerical Fluid Mechanics and Multidisciplinary Design*, pages 129–143. Springer Berlin Heidelberg, 2010.

[70] S. Wagner, R. Bareiss, and G. Guidati. *Wind turbine noise*. Springer, 1996.

[71] G. B. Whitham. *Linear and nonlinear waves*, volume 42. John Wiley & Sons, 2011.

[72] J. F. Williams and D. L. Hawkings. Sound generation by turbulence and surfaces in arbitrary motion. *Philosophical Transactions of the Royal Society of London. Series A, Mathematical and Physical Sciences*, 264(1151):321–342, 1969.

[73] J. Winkler, S. Moreau, and T. Carolus. Airfoil trailing-edge blowing: Broadband noise prediction from large-eddy simulation. *AIAA journal*, 50(2):294–303, 2012.

[74] W. R. Wolf and S. K. Lele. Trailing-edge noise predictions using compressible large-eddy simulation and acoustic analogy. *AIAA journal*, 50(11):2423–2434, 2012.

[75] W. J. Zhu. *Aero-Acoustic Computations of Wind Turbines*. PhD thesis, Technical University of Denmark, 2007.

[76] M. Zhuang and R. Chen. Optimized upwind dispersion-relation-preserving finite difference scheme for computational aeroacoustics. *AIAA journal*, 36(11):2146–2148, 1998.

APPENDIX A

THE FORMULATIONS OF DISPERSION RELATIONS

General dispersion relation of central schemes with $2M + 1$ grid points in x direction of Cartesian coordinates is given as:

$$\frac{\tilde{\alpha}\Delta x}{\alpha\Delta x} = \frac{1}{i\alpha\Delta x}\sum_{l=-M}^{M} a_l e^{il\alpha\Delta x} \tag{A.1}$$

where a_l is the weight of grid points used in finite difference algorithms.

Using Equation A.1, the equations of dispersion relations, which are functions of $\alpha\Delta x$, according to different finite difference algorithms are found as follows:

For standard 2^{nd} order schemes:

$$\frac{\tilde{\alpha}\Delta x}{\alpha\Delta x} = \frac{1}{\alpha\Delta x} sin(\alpha\Delta x) \tag{A.2}$$

For standard 4^{th} order schemes:

$$\frac{\tilde{\alpha}\Delta x}{\alpha\Delta x} = \frac{1}{\alpha\Delta x}\left(-\frac{1}{6} sin(2\alpha\Delta x) + \frac{8}{6} sin(\alpha\Delta x)\right) \tag{A.3}$$

For standard 6^{th} order schemes:

$$\frac{\tilde{\alpha}\Delta x}{\alpha\Delta x} = \frac{1}{\alpha\Delta x}\left(\frac{1}{30} sin(3\alpha\Delta x) - \frac{3}{10} sin(2\alpha\Delta x) + \frac{3}{2} sin(\alpha\Delta x)\right) \tag{A.4}$$

For DRP 4^{th} order schemes:

$$\frac{\tilde{\alpha}\Delta x}{\alpha\Delta x} = \frac{2}{\alpha\Delta x}\left(a_{j=3}\ sin(3\alpha\Delta x) + a_{j=2}\ sin(2\alpha\Delta x) + a_{j=1}\ sin(\alpha\Delta x)\right) \tag{A.5}$$

where $a_{j=1}$, $a_{j=2}$, and $a_{j=3}$ are given in Chapter 2.3.1.